Arabian Journal of Chemistry (2019) **12**, 4675–4693

King Saud University

Arabian Journal of Chemistry

www.ksu.edu.sa
www.sciencedirect.com

ORIGINAL ARTICLE

Arsenic removal by magnetite-loaded amino modified nano/microcellulose adsorbents: Effect of functionalization and media size

Khaled Taleb [a], Jasmina Markovski [b], Zlate Veličković [c], Jelena Rusmirović [d], Milica Rančić [e], Vladimir Pavlović [f,g], Aleksandar Marinković [a,*]

[a] *Faculty of Technology and Metallurgy, University of Belgrade, Karnegijeva 4, 11120 Belgrade, Serbia*
[b] *Vinča Institute of Nuclear Sciences, University of Belgrade, 11000 Belgrade, Serbia*
[c] *Military Academy, 33 General Pavle Jurišić – Šturm Street, Belgrade, Serbia*
[d] *Innovation Center of the Faculty of Technology and Metallurgy, University of Belgrade, Karnegijeva 4, 11120 Belgrade, Serbia*
[e] *Faculty of Forestry, University of Belgrade, Kneza Višeslava 1, 11030 Belgrade, Serbia*
[f] *Faculty of Agriculture, University of Belgrade, Nemanjina 6, 11080 Belgrade-Zemun, Serbia*
[g] *Institute of Technical Sciences of the SASA, Belgrade, Serbia*

Received 13 May 2016; accepted 17 August 2016
Available online 26 August 2016

KEYWORDS

Sorption;
Nanocellulose;
Microcellulose;
Arsenic;
Magnetite

Abstract Comparative adsorption study related to benefits of parent media size, *i.e.* microfibrillated cellulose (**MC**) *versus* nanocellulose (**NC**) support, for the preparation of magnetite (**MG**) based high performance adsorbent for arsenic removal was conducted. Precipitation of **MG** on amino terminal branched organic structure, **L**, either linked by maleic acid residue on **NC** surface (**NC-MA/L**) or linked by oxalyl bridge on **MC** surface (**MC-O/L**) produced **NC-MA/L-MG** and **MC-O/L-MG** adsorbents, respectively. Precipitation of nanosized **MG** on amino functionalized **NC-MA/L** and **MC-O/L**, performed according to optimized procedure, contributed to improved textural properties and adsorptive/kinetic performances of novel adsorbents. Adsorption capacity of arsenate, As(V), was in favor of **NC-MA/L-MG** (85.3 *versus* 18.5 mg g^{-1}) while **MC-O/L-MG** exhibited faster kinetics (0.541 *versus* 0.189 g mg^{-1} min^{-1}). Lower capacity of arsenite, As(III), removal, 68.3 mg g^{-1} for **NC-MA/L-MG** and 17.8 mg g^{-1} for **MC-O/L-MG**, were obtained. Calculated activation energies, 13.28 and 10.87 kJ mol^{-1} for **NC-MA/L-MG** and **MC-O/L-MG** with respect to As(V), respectively, suggest, in accordance with results of Weber-Morris fitting, that internal mass transfer controls

* Corresponding author.
E-mail address: marinko@tmf.bg.ac.rs (A. Marinković).
Peer review under responsibility of King Saud University.

Production and hosting by Elsevier

http://dx.doi.org/10.1016/j.arabjc.2016.08.006

adsorption process. Model free adsorption kinetics confirmed beneficial uses of **MC-O/L-MG** due to low activation energy dependence on the extent of adsorption.

1. Introduction

Arsenic is classified as a Class A human carcinogen, toxic and mutagen and its contamination of drinking water has been a challenge of global magnitude (Ravenscroft et al., 2009). Due to that, exposure to arsenic can cause several skin problems such as pigmentation and hard skin patches, as well as bladder, kidney, lung, liver and prostate cancers (Awual et al., 2012). To limit the exposure to arsenic, the United State Environmental Protection Agency and the World Health Organization promulgated new water standards and decreased the maximum contaminant level (MCL) of arsenic to 10 $\mu g\,L^{-1}$ (Ravenscroft et al., 2009). Subsequently, the strict regulation has initiated extensive development of technologies for effective arsenic removal.

Nowadays, developing of techniques for arsenic removal from water has received extensive attention by environmental scientists. Arsenic removal techniques include coagulation, oxidation, adsorption and reverse osmosis processes, and ion/ligand exchangers (Awual and Jyo, 2009; Awual et al., 2013, 2012, 2011, 2008). Among the possible arsenic removal techniques, adsorption is considered as simple, efficient and economic method which offers flexibility in design and generating high-quality treated effluent. Different adsorbents such as activated carbons, biological materials and mineral oxides were applied (Yousif et al., 2016). In the recent years, ferric (hydr)oxides have attached growing interest in arsenic removal due to their selectivity, chemical stability, low price, availability, and possibility to be produced as nanomaterials with large surface area. In most cases, however, the applicability of the ferric (hydr)oxides nanoparticles is shown to suffer from their poor mechanical strength and tendency to agglomerate. Application of support and production of hybrid materials has emerged as viable option in the preservation of beneficial properties of ferric (hydr)oxide nanomaterials (Hua et al., 2012).

The use of adsorbents containing natural polymers for heavy metals removal through adsorption takes particular attention (Abdel-Halim and Al-Deyab, 2011; Huang et al., 2013; Podder and Majumder, 2019; Sheng et al., 2014; Yousif et al., 2016; Zeng et al., 2015). From the ecological point of view, cellulose is biocompatible, the most widely available and renewable biopolymer available from natural sources (Lavoine et al., 2012). Considering that chemical transformation of hydroxyl groups plays an important role in enhancing the sorption capacity, cellulose proved to be an excellent candidate as support matrix amenable for surface modification (Lavoine et al., 2012; Šimkovic, 2013). Introduction of terminal amino and carboxylic groups provides effective means for ferric (hydr)oxides precipitation. Furthermore, the presence of amino moieties influences the synthesis/-precipitation of ferric oxides and affects the particle size distribution and the colloidal stability in solution (Schwaminger et al., 2015). Functionalized nanosized (Anirudhan and Jalajamony, 2010; Anirudhan et al., 2012; Anirudhan et al., 2015; Donia et al., 2012; Singh et al., 2015; Sun et al., 2014; Yousif et al., 2016; Zhao et al., 2009), as well as microfibrillated cellulose (**MC**) was used for adsorption of As, F, Cr, Pb, Hg, Cu, Ag, U, and organic pollutants (Alila and Boufi, 2009; Aloulou et al., 2006; Hokkanen et al., 2016; Li et al., 2015; Maliyekkal et al., 2010; Tian et al., 2011; Yu et al., 2013). To our best knowledge, there are some reports about the cellulose/ferric (hydr)oxide hybrid materials used for arsenic removal (Zhao et al., 2009), whereas there is no report studying the influence of surface modification/type of functionalities on successfulness of ferric oxides precipitation, their properties and adsorption performances.

However, processing nanocellulose (**NC**) particles and application in a realistic adsorption systems is severely limited by a number of inherent shortcomings: purification, manipulation, and low solubility in organic solvents. Solubility improvement and deaggregation of cellulose particles could be overcome by designing of two general strategies: (1) the covalent functionalization of OH groups at **NC** surface with organic pendant group, and (2) the noncovalent functionalization through supramolecular interactions, which allows the formation of stable **NC** suspensions. More attractive and effective choice is surface covalent modification which could be conducted to introduce high affinity groups for binding/precipitation of the ion/oxides, *e.g.* ferric oxides applicable for arsenic removal. The valuable alternative is design of hierarchical organic structure with numerous terminal amino groups which provide support for efficient precipitation of ferric oxide, control of particle size and adsorbent integrity.

To achieve this goal, amino terminal branched organic structure, **L**, linked either by maleic acid residue on **NC** surface (**NC-MA/L**) or by oxalyl bridge on **MC** surface (**MC-O/L**) was used as support for magnetite (**MG**) precipitation. Design and synthesis of structure **L**, obtained by successive reactions of **NC-MA** and **MC-O** with ethylenediamine (**EDA**), ethylenediamine- tetraacetic acid (**EDTA**) ethyl ester and **EDA** in a final step, produced significant number of amino terminal groups. Nanosized **MG** was deposited/precipitated in an optimized/controlled manner on both **NC-MA/L** and **MC-O/L** surfaces producing **NC-MA/L-MG** and **MC-O/L**-MG adsorbents, respectively. The three main goals of presented study were devoted to elucidation of the benefits of parent media size, **NC** and **MC**, and the extent of the modification of these starting materials, *i.e.* introduction of the number of amino terminal functionalities, and controllable **MG** precipitation on adsorption performances of novel synthesized adsorbents. The specific objectives of the present study were related to comparison of the performances of both adsorbents in terms of the following: (1) textural and morphological properties; (2) adsorption efficiency; (3) kinetics/diffusional processes, and (4) adsorbent affinity to arsenic.

2. Experimental

2.1. Chemicals and materials

Cotton used for NC isolation was supplied from AD. Niva, Serbia (Turkish origin) and microfibrillated cellulose was supplied by Stora Enso Finland. All the chemicals used in this study were of analytical grade and used as received. The following chemicals were supplied from Sigma-Aldrich: sulfuric acid, glacial acetic acid (GAA), toluene, perchloric acid, maleic anhydride (MA), tetrahydrofurane (THF), ethylenediamine (EDA), ethylenediaminetetraacetic acid (EDTA), *N,N*-dimethylformamide (DMF), iron(II) sulfate heptahydrate ($FeSO_4{\cdot}7H_20$), potassium nitrate (KNO_3), potassium hydroxide (KOH), triethylamine (TEA), ethyl oxalyl chloride (EOC), and dicyclohexyl carbodiimide (DCC). The As(V) and As(III) stock solutions were prepared with deionized water (DW), resistivity 18 MΩ cm, using $Na_2HAsO_4{\cdot}7H_2O$ (Sigma-Aldrich) and $NaAsO_2$ p.a. (J.T. Baker, reagent grade), respectively. Sodium metasilicate nonahydrate ($Na_2SiO_3{\cdot}9H_2O$) (p.a.), potassium dichromate ($K_2Cr_2O_7$) (p.a.) and sodium

dihydrogen phosphate (NaH_2PO_4) (p.a.) reagent grade chemicals were purchased from Sigma-Aldrich.

2.2. Adsorbent preparation

The preparation of adsorbents was performed through five consecutive steps applying magnetic stirring (*Heidolph*) and ultrasonic treatment (*Bandello electronic, Berlin, Germany, power 120 W, frequency 35 kHz*) or combination of both methods. Such methodology was applied in order to enhance reactant diffusivity/reactivity due to limited availability of surface functional group being positioned at the internal adsorbent surface. By the use of ultrasound, the liquid circulation and related turbulence generated the formation and collapse of bubbles known as cavitation, thus inducing and improving mass and energy transfer. In this work, ultrasound assisted synthesis proved increased frequency of collision and enhanced reaction efficiency of some reaction steps. In that way, it offers an acceptable alternative for the synthesis of the adsorbents *via* a simple, catalyst-free reaction conditions which help in overcoming rate limiting steps in the course of constructing branched organic structure at **NC** and **MC** surface (Markovski et al., 2014a, 2014b).

2.3. Nanocellulose isolation

Following the procedure of sulfuric acid hydrolysis method (Lu and Hsieh, 2010) for nanocellulose isolation, the **NC** was produced from cotton microfiber (20 g) by treating with sulfuric acid (200 ml, 64 wt.%) at temperature < 40 °C for 1 h. Product was diluted with 800 ml of DW, neutralized to pH 6, and three cycles of centrifugation/DW water washing were applied. After dialyzing for 48 h, nanocellulose was filtered by using polytetrafluoroethylene (45 nm) filter membrane and denoted as **NC**.

2.4. *NC* modification

In order to achieve successful and controlled magnetite precipitation, as well as colloidal stability of cellulose based adsorbent, following amino modification steps were done:

(a) *Modification with maleic anhydride (MA)* – **NC** (10 g) was dispersed in the mixture of glacial acetic acid (100 mL), toluene (130 mL) and perchloric acid (0.5 mL) by the use of ultrasound. Modification of **NC** was performed by dropwise addition of the solution of MA (5 g) in 45 mL of toluene for 15 min under sonication, and followed by maintaining reaction on a magnetic stirrer for 1 h at room temperature. Raw product was washed thoroughly with toluene and ethanol, and vacuum dried at 40 °C for 4 h. Obtained material was denoted **NC-MA**.

(b) ***NC-MA** modification with EDA* – Dispersion of **NC-MA** (10 g) in the 200 mL of tetrahydrofurane (THF) was added slowly into solution of EDA (10 mL) in THF (50 mL) in a three necked flask (500 mL) under ultrasonic treatment. After addition of 2 g of DCC dissolved in 20 mL of THF, the reaction was carried out by combination of ultrasonic/mixing treatment for 30 min (5 min/5 min sonication/mixing cycles), and continued with magnetic stirring at 20–25 °C for 3 h. Product was washed with THF and ethanol (three times), and then vacuum dried at 40 °C for 4 h. This material was denoted **NC-MA/EDA**.

(c) ***NC-MA/EDA** modification with tetraethyl ester of EDTA* – In the dispersion of 10 g of the **NC-MA/EDA** in 200 ml of absolute ethanol, ethanol solution of *N*, *N*′-1, 2-ethanediylbis[*N*-(2-ethoxy-2-oxoethyl)]-1,1′-glycine diethyl ester (tetraethyl ester of EDTA) (27 g) was added slowly. Tetraethyl ester of EDTA was prepared according to literature procedure (Jaeger et al., 2007). Reaction took place under ultrasonic treatment for 10 min, and followed with magnetic stirring at room temperature for 6 h. Product was washed with ethanol, and vacuum dried at 40 °C for 4 h. Obtained material was denoted **NC-MA/EDA-EDTA**.

(d) ***NC-MA/EDA-EDTA** modification with EDA* – **NC-MA/EDA-EDTA** (10 g) was subjected to ultrasound treatment in *N*,*N*-dimethylformamide (DMF) for 5 min, dropwise addition of EDA (10 mL) for 10 min was followed by heating/mixing at magnetic stirrer for 2 h at 50 °C. Obtained product was washed by using abundant quantity of DMF and DW, and dried at 60 °C for 12 h under vacuum. Synthesized material was denoted as **NC-MA/EDA-EDTA-EDA** (**NC-MA/L**).

2.5. Synthesis of NC-MA/EDA-EDTA-EDA-MG adsorbent (*NC-MA/L-MG*)

In order to achieve optimized method of **NC-MA/L-MG** synthesis and shorten experimental procedure the Response Surface Methodology (RSM) was applied for designing of the optimization of MG precipitation on **NC-MA/L** (Table S1; Supplementary data). The **NC-MA/L** (10 g) was dispersed in 100 mL $FeSO_4{\cdot}7H_2O$ solution of different concentrations: 0.013, 0.04, 0.1, 0.13, 0.16, 0.19, 0.23, 0.27, 0.32, 0.35, 0.39 and 0.49 mol L^{-1} performed ultrasonic treatment under inert atmosphere (N_2) for 10 min. After sonication NC dispersion was transferred to oil bath, with constant gentle mixing, and temperature was adjusted at 90 °C using magnetic stirrer/heater. Afterward, 45 mL of oxygen-free solution containing different quantities of reactants: from 0.03 g to 1.1 g KNO_3, and from 0.2 g to 7.6 g KOH, calculated according to literature method (Schwertmann and Cornell, 2000) with respect to starting $FeSO_4{\cdot}7H_2O$, was added during 30 min providing continuous iron oxide precipitation. After precipitation, reaction was heated for additional 60 min at 90 °C, and left overnight. The adsorbent **NC-MA/L-MG** was isolated in the form of black precipitate, washed with DW until getting free from ions in filtrate and vacuum dried at 40 °C for 6 h. For the comparative purpose a sample of **MG** was prepared according to literature method (Schwertmann and Cornell, 2000).

2.6. Synthesis of *MC-O/L-MG* hybrid adsorbent

MC (10 g) was soaked in a mixture of dry THF (250 mL) and triethylamine (TEA) (30 mL) followed by dropwise addition of ethyl oxalyl chloride (EOC) (30 mL) in dry THF (50 mL). Reaction was sonicated for 1 h at room temperature. Isolated

product ethyl oxalyl modified **MC**, **MC-O**, (10 g) was used as a media for linkage of **EDA-EDTA-EDA** structure in an analogous manner as it was performed for **NC-MA/L**. In that way, **MC-O/L** modified microfibrillated **MC** material was obtained. **MC-O/L** was subsequently modified with **MG** in the way analogous to preparation of **NC-MA/L-MG** adsorbent (Section 2.5). RSM experimental plan (Table S1; Supplementary data) was designed according to determined total basic sites at **MC-O/L** surface (0.60 mmol g^{-1}; Section 3.1).

2.7. Solvent/nonsolvent (water/xylene) system applied for controllable impregnation of the NC-MA/L and MC-O/L with magnetite

The results of the optimization procedure were applied for the controllable impregnation of **MG** on **NC-MA/L** support in a solvent/nonsolvent system. **NC** (10 g) was soaked with xylene (non-solvent used to provide continual medium and wetting of the **NC** material; mixing of the medium was achieved by nitrogen/air bubbling in a upstream flow) in a perforated column with gas inlet/outlet valves, solvent exhaustion valve and system for vacuum drying of the **NC** at different modification steps. After establishment of continuous flow of nitrogen through two phase systems xylene/**NC-MA/L** and xylene/**MC-O/L**, slow addition (15 min) of the 40 mL (0.95 mol L^{-1}) and 20 mL (0.85 mol L^{-1}) of $FeSO_4{\cdot}7H_2O$ solution, respectively, started from dropping funnel situated at the top of column. Fine distribution of the $FeSO_4{\cdot}7H_2O$ solution was achieved by the glass frit assembled at the funnel. Small droplets of water iron solution were attracted by hydrophilic **NC-MA/L** and **MC-O/L** surface (concomitantly forced by non-solvent), and nitrogen bubbling promoted formation of uniform film at suspended material surface. Optimization of the water quantity was performed in a batch system in order to provide fulfillment of porous structure and formation water film at outer surface. Modification of NC surface with hydrophilic amino groups helps surface wetting and more importantly, the interaction of Lewis acid (iron ion) with Lewis base site (amino groups) provides initial nucleation center for magnetite precipitation. It was performed by continual bubbling of N_2 at 90 °C, and by dropwise addition of an oxygen-free solution of 20 mL (0.86 g KNO_3 and 5.95 g KOH) or 10 mL (0.38 g KNO_3 and 2.65 g KOH) or for 20 min into dispersions of xylene/**NC-MA/L** and xylene/**MC-O/L** impregnated with appropriate quantity of $FeSO_4{\cdot}7H_2O$, respectively. After precipitation, the reaction was heated for additional 60 min and cooled overnight. The adsorbent **NC-MA/L-MG** and **MC-O/L-MG** were isolated as black precipitate, washed with DW until getting free from sulfate ion in filtrate and dried. No sieving was necessary to apply for material obtained by this method. The multistep syntheses of **NC-MA/L-MG** and **MC-O/L-MG** adsorbents are illustrated in Fig. 1.

2.8. Characterization of adsorbents

Analysis of textural properties of obtained materials was performed by using **B**runauer-**E**mmett-**T**eller (BET) method for the determination of the specific surface area, and the **B**arrett-**J**oyner-**H**alenda (BJH) method for the determination of the mesoporosity parameters. The X-ray diffraction (XRD) (BRUKER D8 ADVANCE) was used for phase and structural analysis of adsorbents. The surface morphology was examined by field emission gun scanning electron microscopy (FEG–SEM) with a field emission gun TESCAN MIRA3 XMU electron microscope and scanning electron microscope (SEM) by using JEOL JSM-6610LV. Distribution of nanoparticles on cellulose surface was further verified using transmission electron microscope (JEOL JEM-1400). Fourier-transform infrared spectra (FTIR) were collected on BOMEM (Hartmann & Braun) spectrometer and were employed to determine the surface groups and its interactions with arsenate. Raman spectra were collected with a XploRA Raman spectrometer from Horiba Jobin Yvon. The system employed laser at 532 nm (maximum output power 20–25 mW). The thermal stability of the samples was investigated by simultaneous non-isothermal thermo-gravimetric analysis (TGA) using a SETARAM SETSYS Evolution 1750 instrument. The measurements were conducted at a heating rate of 10 °C/min in argon or air atmosphere (flow rate was 20 mL/min) in the temperature range of 30–700 °C. Determination of amino group was performed according to the literature volumetric method and degree of amination obtained by Kaiser test (DA_{Kaiser}) (Vuković et al., 2011). The pH values at the point of zero charge (pH_{PZC}) of the samples, *i.e.* the pH above which the total surface of the samples is negatively charged, were measured using the pH drift method (Erdem et al., 2004; Vuković et al., 2011). Quantification of the available amino group was determined by applying Kaiser test (DA_{Kaiser} – degree of amination obtained by Kaiser test (Tian et al., 2011), and by volumetric method (Vuković et al., 2011). The acid value (AV) was determined according to ASTM D3644 standard, and presented as mg KOH g^{-1} per gram of specimen.

The arsenic concentrations in the solutions after the adsorption and kinetic experiments were analyzed by inductively coupled plasma mass spectrometry (ICP-MS), using an Agilent 7500ce ICP-MS system (Waldbronn, Germany). ICP-MS detection limit was 0.030 μg L^{-1} and the relative standard deviation (RSD) of all arsenic species investigated was between 1.3 and 5.1%.

2.9. Batch adsorption experiments

Batch adsorption experiments were conducted in a 100 mg L^{-1} suspension with 10 mL of arsenate solution at pH 6.0 ± 0.1. Adsorption equilibrium and kinetic experiments were performed by varying initial arsenic concentrations: 0.10, 0.30, 0.50, 0.60, 1.0, 2.0, 3.0, 5.0, 7.0, 10.0, 15.0 and 20.0 mg L^{-1} at three temperatures of 298, 308 and 318 K. The initial pH (pH_i) values were adjusted by addition of 0.5 mol L^{-1} HCl or 0.5 mol L^{-1} NaOH solutions. A laboratory pH meter, *Mettler Toledo FE20/FG2* (*Switzerland*), with an accuracy of ±0.01 pH units, was used for the pH measurements. The systems were equilibrated at different rates of stirring, 100–150 rpm. The effect of contact time on adsorption kinetics was studied in the range 2–360 min at C_i = 100 μg L^{-1}, and 90 min was selected as optimal time. Competitive kinetic study was conducted with 0.1 mg L^{-1} of silicate, chromate and phosphate solutions, contact time 90 min and m/V = 100 mg L^{-1}. The sample solutions were filtered through a Millipore 0.22 μm membrane filter (*Bedford, USA*) and analyzed on **I**nductively **C**oupled **P**lasma **M**ass **S**pectrometry (ICP-MS). The arsenic uptake of adsorbents was evaluated by the use of mass balance Eq. (1):

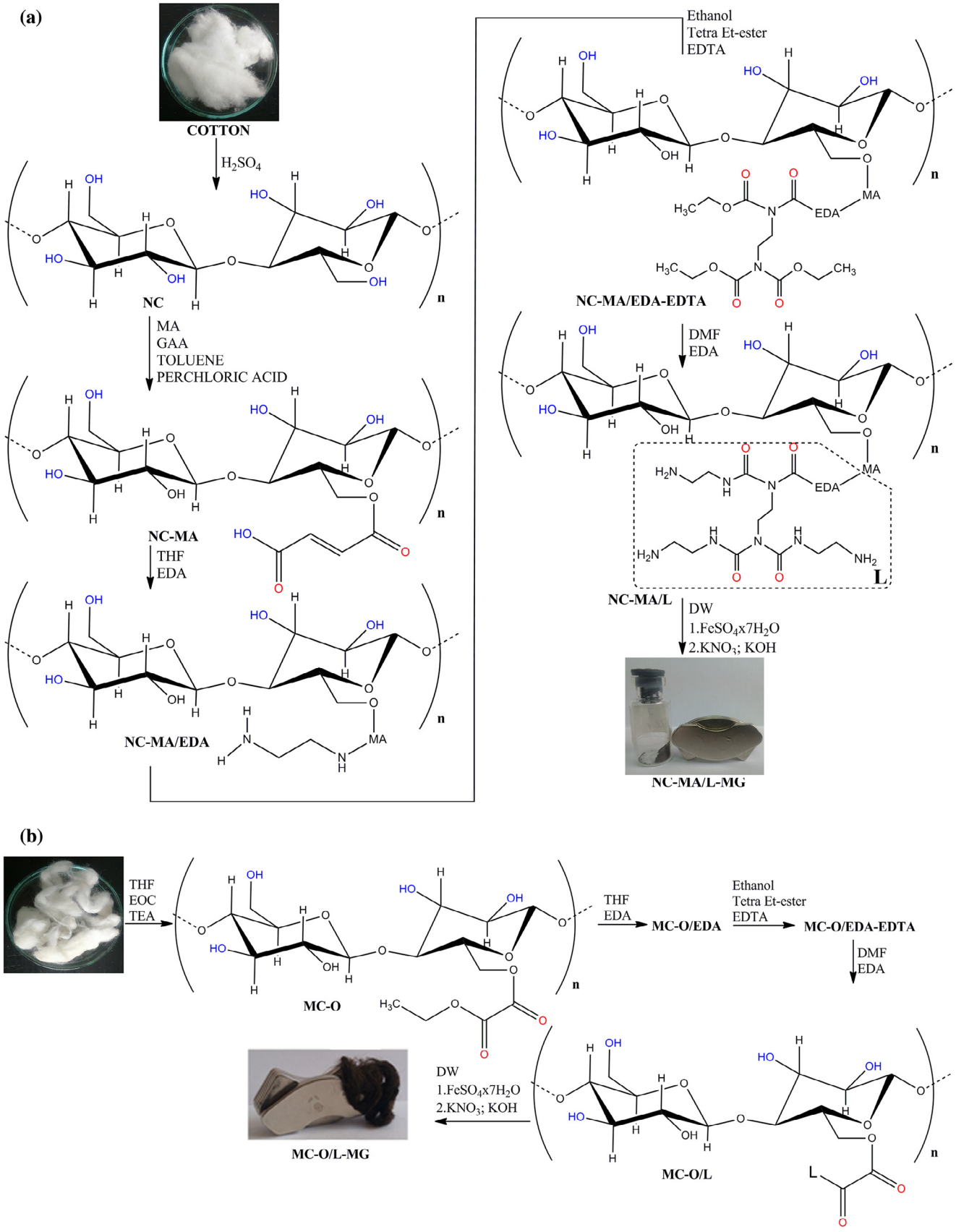

Figure 1 Modification paths applied for **NC-MA/L-MG** (a) and **MC-O/L-MG** (b) adsorbents synthesis.

$$q = \frac{C_i - C_f}{m} V \quad (1)$$

where q is adsorption capacity in mg g^{-1}, C_i and C_f are initial and final arsenic concentrations in mg L^{-1}, V is volume of the solution in dm^3, and m is mass of adsorbent in g. All the experimental data presented were determined by using ICP-MS techniques, a given as mean values from three determinations. Results showed that the adsorption of arsenic on the container wall and filters was negligible.

The degree of conversion (degree of adsorption) could be expressed by a dimensionless number defined by Eq. (2):

$$\alpha(t) = (C_i - C_t)/(C_i - C_f) \quad (2)$$

where C_t is the concentration of arsenic at elapsed time of adsorption t, and this expression is used for calculation of the extent of adsorption.

To evaluate the regeneration capabilities, after adsorption experiments and washing with DW, wet adsorbents (m/V = 100 mg L^{-1}) were redispersed in 20 mL of the solution used for desorption (NaOH/NaCl, 0.5/0.5 mol L^{-1}). The amount of desorbed As(V) was measured after magnetic mixing for 3 h in a batch system. Five consecutive adsorption/desorption cycles were performed in triplicate.

2.10. Response surface methodology (RSM): experimental design of adsorbent preparation

Full data on applied RSM methodology are given in Supplementary data.

2.11. Statistical criteria used for the evaluation of the goodness of the modeling

Statistical methods applied for evaluation of the fitting are given in Supplementary data.

3. Results and discussion

3.1. Optimization of the adsorbents synthesis

In order to design effective, reusable and selective hybrid adsorbents for As removal an optimization study was conducted. Optimization goals were directed to syntheses of adsorbent with high capacity/efficiency, improved chemical and mechanical stability of **MG** deposit, and fast adsorption of arsenic at operational time scale. The optimization procedure, performed according to Sections 2.5 and 2.6, and according to experimental plan presented in Table S1, revealed that optimal performance was obtained by using the following:

- 100 mL of $FeSO_4 \cdot 7H_2O$ (0.38 mol L^{-1}) and 45 mL of pH adjustment solution (5.95 g KOH and 0.86 g KNO_3) for **NC-MA/L-MG** adsorbent synthesis (Fig. 2(a)), and
- 100 mL of $FeSO_4 \cdot 7H_2O$ (0.17 mol L^{-1}) and 45 mL of pH adjustment solution (2.65 g KOH and 0.38 g KNO_3) used for **MC-O/L-MG** adsorbent synthesis (Fig. 2(b)).

Results of the optimized procedure of adsorbent syntheses in a batch system (Sections 2.5 and 2.6) were applied, with an adjustment of the volume of used solution to provide reaction in a water thin/hydrophylic precursor material, for syntheses of **NC-MA/L-MG** and **MC-O/L-MG** adsorbent according to methodology described in Section 2.7. In that way, the highest adsorption capacities were obtained at ~29% loaded iron oxide in **NC-MA/L-MG** and ~13% in **MC-O/L-MG** (Fig. 2(c)).

The most probable structure of designed intermediates and adsorbents is presented in Fig. 1. Significance of the amino groups involved in the complexation was recently unequivocally presented (Cabaniss, 2011). Cations are strongly bonded to amino groups, by complexation/-chelation interactions, and higher nucleophilicity of amino groups, at pH > pH_{PZC}, brings to stronger interaction with cation (Vuković et al., 2011). In that sense, it was of utmost interest to introduce number of amino groups through hierarchical branching of organic structure covalently bonded to **NC** and **MC** surface (Fig. 1). The total basic sites, 0.60 and 1.02 mmol g^{-1} found for **MC-O/L** and **NC-MA/L**, respectively, contributed to uniform/high **MG** loading. According to total basic sites determination, it was evaluated that ~19 and ~11 wt.% of introduced organic functionalities are present in **NC-MA/L** and **MC-O/L**, respectively. Modification of **NC**, with an acid value (AV) of 28, by MA to **NC-MA**, introduced ~1.50 mmol g^{-1} of carboxylic group (AV = 150). Lower efficiency of **NC-MA** modification with EDA resulted in 0.92 mmol g^{-1} of amino group (~61% conversion) in **NC-MA/EDA**. Despite that according

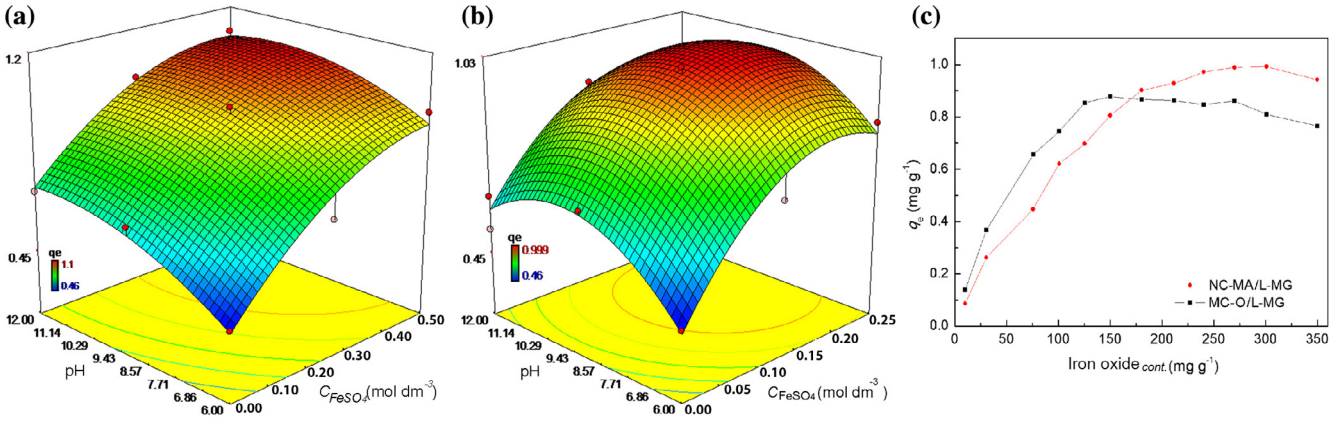

Figure 2 Contour diagram representing adsorbent capacity *versus* C_{FeSO4} and pH in the synthesis of **NC-MA/L-MG** (a), **MC-O/L-MG** (b), and capacity of both adsorbents *vs* amount of iron oxide (c).

to stoichiometric ratio considered for subsequent modifications of **NC-MA/EDA** to **NC-MA/L** (Fig. 1), 2.76 mmol g^{-1} of amino groups should be expected, and experimental value of 1.02 mmol g^{-1} was found. This indicates lower efficiency of modification introducing amino groups, present at **NC-MA/EDA** surface, due to steric hindrance of introduced voluminous tetraethyl ester of EDTA structure. Generally, optimal procedure for **MG** precipitation/complexation on **NC-MA/L** and **MC-O/L** was defined by using RSM methodology, was successful, according to Sections 2.5 and 2.6, but controlled precipitation and uniform distribution of **MG** on **NC-MA/L** and **MC-O/L** surface were achieved according to Section 2.7.

3.2. Characterization of the adsorbents

3.2.1. Textural properties and pH_{PZC}

Multi-step synthesis of adsorbents was applied in order to design the material with an appropriate geometry, surface properties and pore structure. The textural properties and zero point of charge (pH_{PZC}) before and after adsorption are summarized in Table 1.

Due to dimensional differences of parent materials, the higher value of specific surface area and pore volume was in favor of **NC-MA/L-MG**, while higher pore diameter was found for **MC-O/L-MG** compared to the raw **MG**. Literature data of unmodified nano- and micro fibrillated cellulose (Dufresne, 2012), showed that differences in surface area and pore diameter are generally influenced by the textural properties of substrate, applied modification method as well as post processing of obtained material. In contrast to mild thermal treatment applied for **NC-MA/L-MG** and **MC-O/L-MG** production, high temperature processing exerts significant change in textural properties of final material. The surface area and pore volume of thermally treated silica, after ligand immobilization, showed significant decrease in textural properties (Awual, 2015; Awual et al., 2016a, 2016b; Awual, 2016a, 2016b, 2016c). Regardless of obtained results both methodologies could find application in production of adsorbents of different properties. Precipitation of **MG** on **NC-MA/L** and **MC-O/L** provided such conditions applicable for preservation of organic branched structures with controllable deposition of nanoscale materials. The shift of pH_{PZC} value (Table 1) indicates specific arsenate adsorption rather than electrostatic interaction, and formation of complexed/precipitated arsenic species at surface of magnetite based adsorbent is a main adsorption mechanism (Markovski et al., 2014a, 2014b).

3.2.2. XRD analysis

XRD diffractograms of **NC** and **NC-MA**, presented in Fig. 3 (a), provide insight into structural changes in the course of **NC** modification. An increase in crystallinity of **NC-MA** was observed. Both diffractograms display two well-defined peak doublets around $2\theta = 20°$ and 22.0° which correspond to (200) plane of cellulose crystal structure. Those doublets indicate the existence of cellulose I and cellulose II allomorphs (Peng et al., 2013). Modification with MA causes sharper signal, and increases contribution of cellulose II crystallites, and overall degree of crystallinity. In the sample of **NC-MA** signal at 12.24° corresponds to (−110) crystal plane of cellulose I (Klemm et al., 2011). The signal at 35.0° showed higher intensity for **NC-MA**, corresponds to (004) atomic plane of cellulose I (Peng et al., 2013). Also, it was shown that appearance of new crystalline peaks at $2\theta \sim 35°$ as well as at 41.0° indicates the increase in the crystallinity of NC-MA (Maiti et al., 2013).

Phase and structural analysis of **NC-MA/L-MG** and **MC-O/L-MG** confirmed the presence of **MG** (Fe_3O_4), as it was indicated by peak at 30.16, 35.52, 37.16, 43.17, 54.22, 57.10, 62.70° (JCPDS 19-629) (Fig. 3(b)). Differences in peak broadness and intensity indicate lower degree of crystalline phase of embedded **MG** in **MC-O/L-MG**. The mean crystallite size, calculated by using Scherrer equation based on the half width of the most intense peaks in XRD patterns, indicates 22 and 19 nm of grain sizes of **MG** present on **NC-MA/L-MG** and **MC-O/L-MG** surface, respectively. These values are somewhat lower than ones observed by transmission electron microscopy (TEM) (Fig. 7). A somewhat lower crystallite size, found for **MC-O/L-MG**, is due to lower number of amino groups (crystallization centers) accessible for iron coordination. Obtained results indicated the high coverage of **NC-MA/L** and somewhat lower for **MC-O/L** by **MG**. Due to the known fact that **MG** and maghemite (γ-Fe_2O_3) have similar XRD pattern it was necessary to apply Raman spectroscopy in order to clearly distinguish nanocrystalline form of deposited iron oxide.

3.2.3. Raman spectroscopy

Raman spectra of the **NC**, **NC-MA/L** and **NC-MA/L-MG**, and **MC** and **MC-O** are shown in Fig. 4. The region below 1750 cm^{-1}, observed at Raman spectra of **NC** and **NC-MA/L**, originates from the conformation of cellulose skeleton, while the region above 2888 cm^{-1} and higher than 3000 cm^{-1} originates from hydrogen bonding of OH group (Szymańska-Chargot et al., 2011). Comparing the Raman spectra of the **NC** and **NC-MA/L**, the overlapped bands, observed in the region 3215–3405 cm^{-1}, are due to OH and NH_2 stretching vibration (Gabelica, 1976). Also, the signals at 1456 cm^{-1} and 1473 cm^{-1}, a characteristic for methylene bending modes of two stereo-chemically nonequivalent CH_2OH groups of the crystalline NC skeletons, merge into one single signal at 1456 cm^{-1} in **NC-MA/L**. This change explained the differences

Table 1 Textural properties, pH_{PZC} of **MG**, **NC-MA/L-MG** and **MC-O/L-MG** adsorbent.

Adsorbent	Specific surface area (m^2 g^{-1})	Pore volume (cm^3 g^{-1})	Pore diameter (nm)	pH_{PZC}[a]	pH_{PZC}[b]
MG	66.7	0.85	12.3	6.6	5.9
NC-MA/L-MG	85.3	0.71	15.2	6.5	5.7
MC-O/L-MG	35.5	0.45	18.4	6.1	5.8

pH_{PZC} of **NC** was found to be < 1, and pH_{PZC} of **NC-MA** < 3.
[a] Before adsorption.
[b] After adsorption.

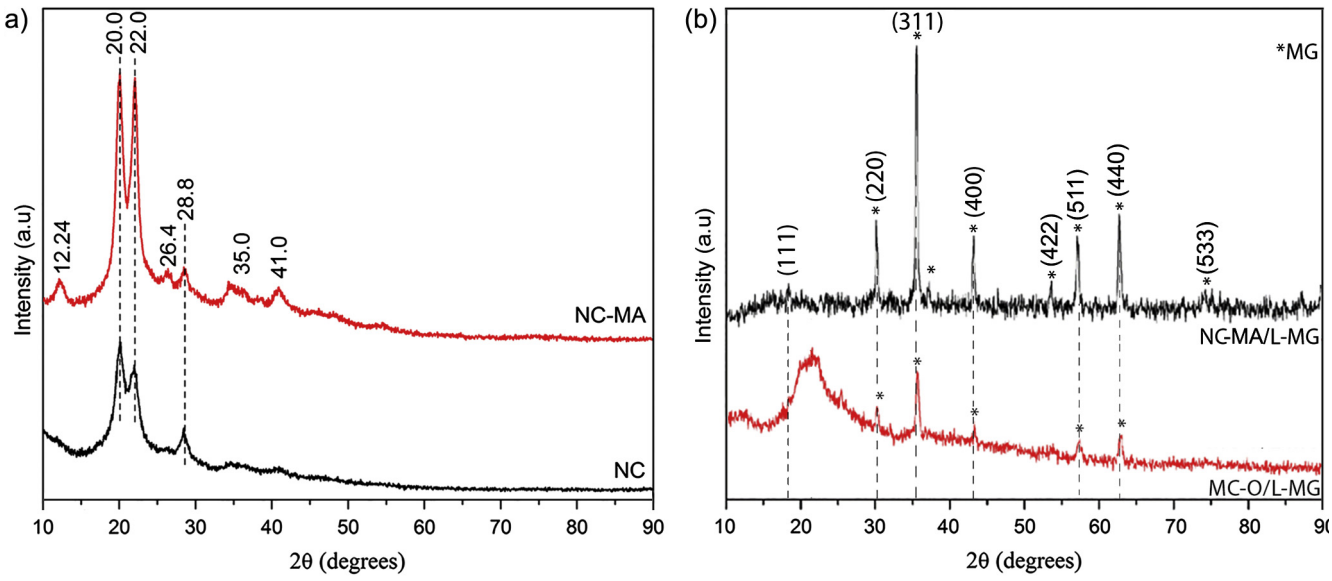

Figure 3 XRD diffractograms of (a) **NC** and **NC-MA**, and (b) **MC-O/L-MG** and **NC-MA/L-MG**.

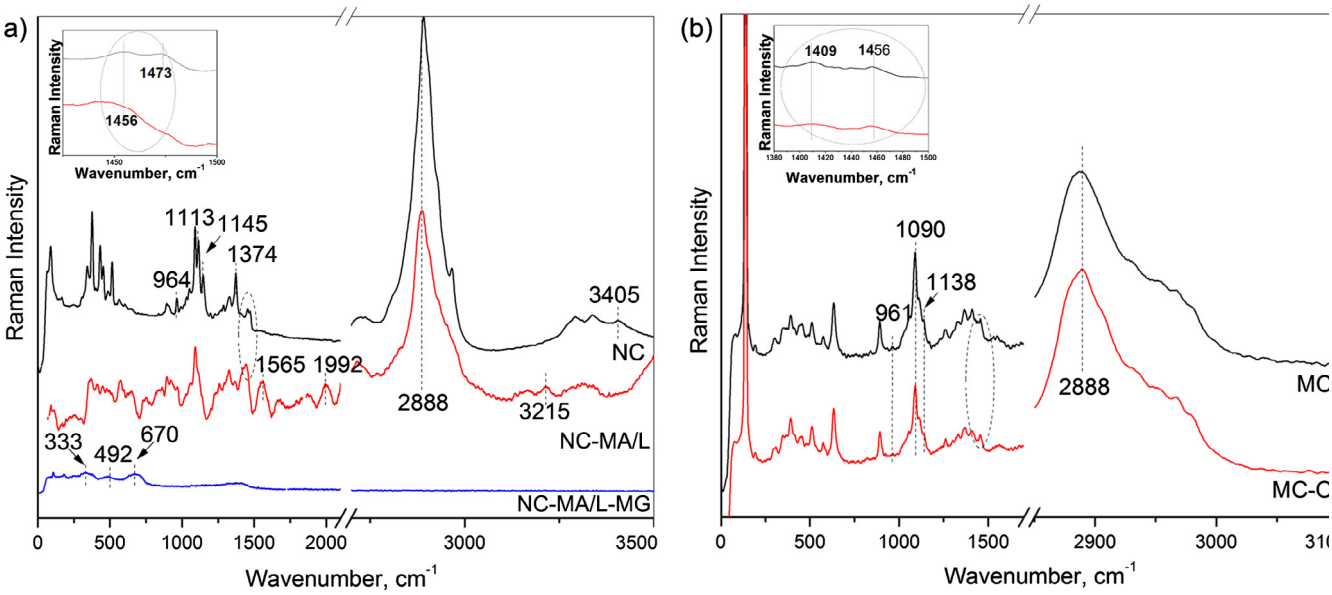

Figure 4 Raman spectra of (a) **NC**, **NC-MA/L** and **NC-MA/L-MG**, and (b) **MC** and **MC-O**.

between the vibrational behavior of crystalline and amorphous domain in **NC** (Schenzel et al., 2005), and indicated transition from crystalline to amorphous form of these two CH_2 bending modes during surface modification (Schenzel and Fischer, 2001; Wiley and Atalla, 1987). Also, the intensity of the characteristic peak of highly crystalline **NC** (1473 cm^{-1}), and other signals decrease in comparison with amorphous **NC-MA/L** domain.

Weak bands, observed in region from 964 cm^{-1} to 1113 cm^{-1}, originate from C6 atom bending vibrations (H—C—C and H—C—O), while the strong stretching vibration of unhydroglucose skeleton is observed at 1145 cm^{-1} (C—C, C—O and C—O—C) (Schenzel et al., 2005; Wiley and Atalla, 1987). The NC backbone deformation vibration bands, δ (CH_2), δ(HCC), δ(HCO) and δ(COH), are observed at 1374 cm^{-1} (Zhang et al., 2011). Wide bands observed in the region between 1565 cm^{-1}–1992 cm^{-1} and 900 cm^{-1}–1500 cm^{-1} originate from the **MA** and **EDTA** moieties in **NC-MA/L**, respectively.

The non-polarized spectrum of **NC-MA/L-MG** shows magnetite predicted phonon bands as characteristic peak at 670 cm^{-1} (Shebanova and Lazor, 2003). Due to susceptibility of **MG** to transform into maghemite, under exposure to laser, two weak peaks appeared at 350 and 500 cm^{-1}. The absence of **NC** characteristic bands in **NC-MA/L-MG** spectrum indicates homogenous distribution/entire surface coverage by deposited **MG** on amino functionalized **NC**.

The Raman spectra of the **MC** and **MC-O** showed similar peak structure and position, except that cellulosic structure

of **MC** basis participates at higher extent in response to laser impulse. Regardless of adjustment of laser power the Raman spectrum of **MC-O/L-MG** sample was not obtained.

3.2.4. FTIR spectroscopy

The FTIR spectra of intermediates and adsorbents, before and after arsenate adsorption, are presented in Fig. 5. From the FTIR spectra of all intermediates, a broad band about 3423 cm^{-1} ascribed to OH and NH stretching vibrations can be observed. Adsorption of arsenate oxyanions causes shifting of the stretching vibration of OH band to 3451 cm^{-1}. Differences in the peak intensity, peak shifting and appearance of peak after adsorption indicate arsenate bonding by appropriate functional groups. Carbonyl group absorption at 1714 cm^{-1}, found in **NC-MA**, is missing in the spectrum after **MG** modification. Absorption peak, at 1635 cm^{-1}, originates from deformation vibrations of OH bond, and is negligibly shifted to 1637 cm^{-1} after **MG** modification. Broad bands at ≈1714 and ≈1635 cm^{-1}, are shifted to ≈1637 cm^{-1}, in **NC-MA/EDA** and **NC-MA/L**, a band corresponding to amide stretching vibration (amide I) coupled with in-plane N—H deformation vibration. The bands in the region 750–1000 cm^{-1}, and one at 1373 cm^{-1}, show the presence of sulfonates and amino groups (Socrates, 2004). The strong bands at 582 cm^{-1}, assigned to Fe—OH vibrations present at **MG** surface, after arsenate adsorption appeared at 617 cm^{-1}. This region corresponds to vibration of As—O—Fe complexed/precipitated arsenate species, and at different surface coverages, bidentate binuclear and mononuclear monodentate complex could be formed, where As—OH free bonds are present as unprotonated and/or protonated depending on pH (Markovski et al., 2014a, 2014b; Grossl et al., 1997).

3.2.5. Thermal analysis (TGA)

The success of nano/microcellulose modification and thermal stability of composites constituent was evaluated by the use of TGA. TGA and differential thermal analysis (DTG) curves, recorded for **NC**, **MC**, **NC-MA/L**, **NC-MA/L-MG** and **MC-O/L-MG**, are shown in Fig. 6. The TGA curve and DTG peaks, observed at 258 °C for **NC** and 260.5 °C for **MC**, indicate similar thermal behavior of both materials in whole temperature range. As it can be observed, the thermal decomposition of **NC** and **MC** occurred in three steps: (i) 30–225 °C, (ii) 225–325 °C, and (iii) 325–700 °C range. In the first stage, ~5% and ~11% weight loss were observed due to dehydration of **NC** and **MC**, respectively. In the second stage, almost 61% mass loss occurred due to the splitting/thermal decomposition of cellulose structure, *i.e.* chain scission which evolves gaseous products leaving condensation/carbonaceous residues. After 325 °C, 20% and 18% weight loss were observed due to the degradation of the **NC** and **MC** condensed carbonaceous material, respectively. The end of first region is shifted to the lower temperature (145 °C) for the **NC-MA/L** sample. Also, the weight loss difference, ~12%, between **NC** and **NC-MA/L** **is** similar to evaluated organic fraction, obtained according to amino groups calculation ~18% (Section 3.1). DTG peak for **NC-MA/L** occured at 158 °C refers to dehydration and evaporation of residual solvents, while DTG peak at 273.4 °C refers to cellulose backbone decomposition.

The higher stability, comparing to **NC** and **MC**, and similar thermal behavior of **NC-MA/L-MG** and **MC-O/L-MG** were noticed (Fig. 6(a)). Higher thermal stability is due to contribution of **MG** protective layer which forms, by sintering of **MG** nanocrystallite, a stable core shell-like structure. The first stage of mass loss (< 300 °C) is due to removal of physically adsorbed water, residual reactants and amorphous cellulose domain. The weight loss in the range from 300 to 450 °C is ascribed to the rapture of weak head to head acetal linkage between cellobiose units in an amorphous/lower crystallinity domain of cellulose. Corresponding DTG peaks could be observed at 306.8 °C, 324.6 °C and 379 °C for **MC-O/L-MG** and 394.2 °C for **NC-L-MG**, respectively. The third stage, at > 400 °C, takes place by random scission/gradual decomposition of main cellulose polymeric chain. A residual inorganic material of 42% and 28% in an inert atmosphere, and comparative experiments in air showed that 33% and 17% residuals in **NC-L-MG** and

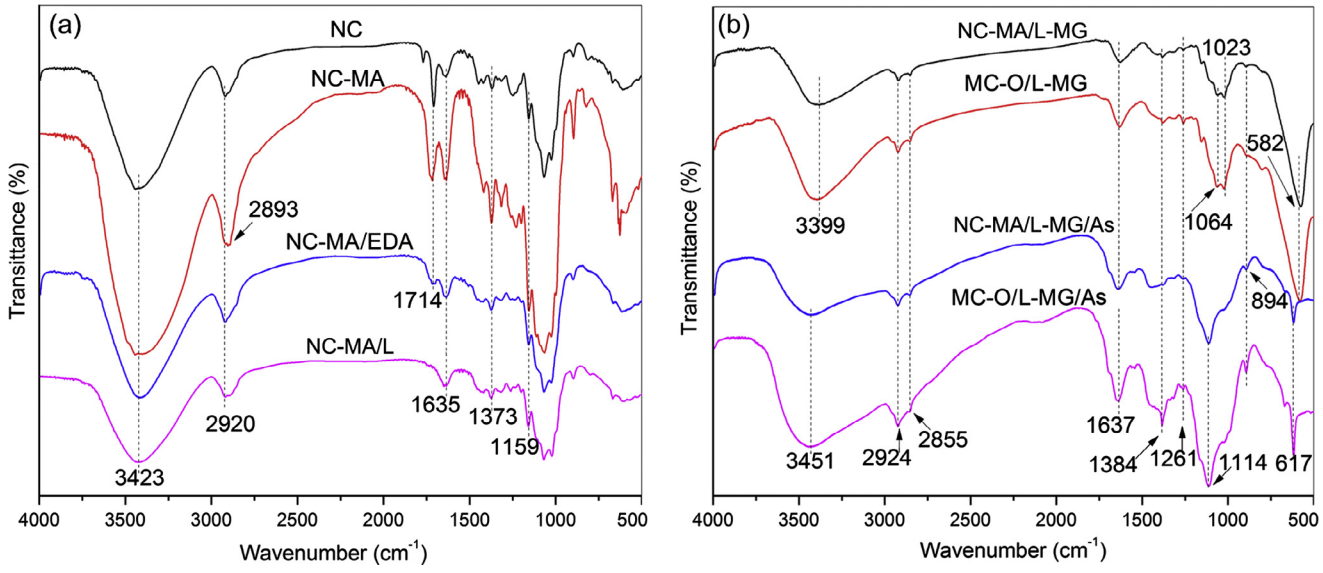

Figure 5 FTIR spectra of (a) **NC**, **NC-MA**, **NC-MA/EDA** and **NC-MA/L** and (b) **NC-MA/L-MG**, **MC-O/L-MG**, **NC-MA/L-MG/As** and **MC-O/L-MG/As**.

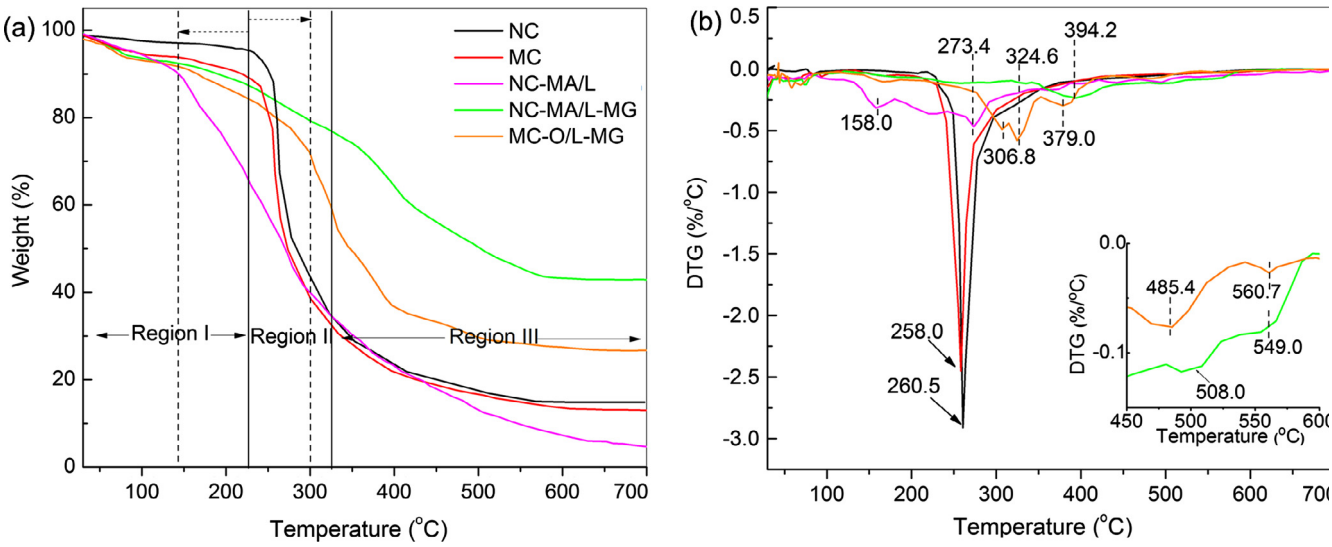

Figure 6 TGA (a) and DTG (b) curves of **NC**, **MC**, **NC-MA/L**, **NC-MA/L-MG** and **MC-O/L-MG**.

MC-O/L-MG were obtained, respectively. On the DTG curves of **NC-L-MG** and **MC-O/L-MG** peaks observed at temperatures >470 °C refer to thermal oxidation and dehydroxylation of precipitated magnetite (Przepiera and Przepiera, 2001).

3.2.6. Morphological characterization

The morphology of the synthesized adsorbents was analyzed by using SEM/FEG–SEM techniques, results given in Fig. 7(a), (b), (d) and (e), while TEM results are given in Fig. 7(c) and (f).

Morphology of **NC-MA/L** (Fig. 7a) indicated surface coverage by organic material due to chemical modification, and subsequent **MG** deposition affects the morphological structure of the surface of **NC-MA/L-MG** (Fig. 7b). SEM micrograph of **NC-MA/L-MG** adsorbent obtained at lower magnification is shown in Fig. S1 (Supplementary material).

SEM micrograph of **MC-O/L-MG** adsorbent is given in Fig. 7(d) and (e). The evaluated average diameter of **MC**, **MC-O** and **MC-O/L-MG** was in the range 30 ± 1.2 μm. The modified **MC** fibers showed small diameter changes of parent cylindrical strands due to organic modification and **MG** precipitation at **MC-O/L** surface. Evolution of the **MC-O/L-MG** morphology can be explained by heterogeneous reaction which takes place by **MG** precipitation on terminal amino branched structure with incorporated **NC** grains on the fiber surface.

TEM analysis (Fig. 7(c) and (f)) confirmed nanoscale dimension and irregular distribution of cubic **MG** nanoparticles onto irregular/porous morphology of **NC-MA/L** and **MC-O/L**. It can be concluded that morphology of **NC-MA/L-MG** and **MC-O/L-MG** adsorbents is the result of both physical structure of nano/microscale material, and chemical structure/properties of functional groups present at **NC-MA/L** and **MC-O/L** surface.

3.3. Adsorbents performance in non-competitive conditions

3.3.1. pH-dependent, equilibrium, thermodynamic and competitive adsorption study

Considering significance of pH influences on arsenic speciation and ionization state of adsorbent surface, it was important to study influence of pH (in the range 3–10) on effectiveness of As removal. The results of the pH-dependent adsorption study, *i.e.* arsenate removal *versus* initial pH (pH_i) for both **NC-MA/L-MG** and **MC-O/L-MG** adsorbents, and change of final pH (pH_f) in relation to initial pH (pH_i) are shown in Fig. 8(a). The extent of adsorption pH_f/pH_i relation is affected by both release/consumption of hydrogen ions, *i.e.* protonation/deprotonation of **MG** surface, and pH-dependent arsenic speciation. These factors determine that effective As(V) adsorption was obtained in pH range 3.0–7.0 (Fig. 8(a)), while pH_f/pH_i relationship indicates similar arsenic adsorption mechanism with respect to both adsorbents. Similar behavior was found for As(III) pH-dependent adsorption (Fig. S2).

The p*K*a values of arsenic acid: $pKa_1 \sim 2.3$, $pKa_2 \sim 7.0$ and $pKa_3 \sim 11.5$, indicate that molecular form mainly exists in a solution at pH < 2.0, and pH-dependent equilibrium of anionic species, $H_2AsO_4^-$ or $HAsO_4^{2-}$, exists at pH in the range 2–10 (Fig. S3) (Issa et al., 2011). At $pH_i < pH_{PZC}$ (Table 1), the protonation of surface functional generates positive charge which contributes to favorable bonding of negatively charged arsenate ions (Fig. S3). Both surface state and As speciation play significant contribution to electrostatic interaction (attraction/repulsion) between surface/ions causing intensity of As flux toward the specific adsorption sites. Enhancement of electrostatic attraction is thus highly feasible for As(V) species, while it is of minor importance for the neutral form of arsenous acid (Fig. S3). At $pH_i > pH_{PZC}$, deprotonation of surface functional groups, increased concentration of negatively charged arsenic species and competition of hydroxyl ion at higher pH contributed to enhanced repulsion at the boundary layer of the adsorbent interface, *i.e.* lower adsorption efficiency is a consequence.

Simultaneous determination of arsenic and iron by ICP-MS showed that at pH < 5 significant dissolution of **MG** precipitate was noticed. Good adsorption capacity and noticeable iron dissolution at pH < 5 dictated that selection of pH 6.0 was the best choice, and this pH was used in subsequent adsorption experiments.

The state of adsorption equilibrium was analyzed by fitting experimental data with various isotherm models (Foo and Hameed, 2010) by applying nonlinear least squares fitting to

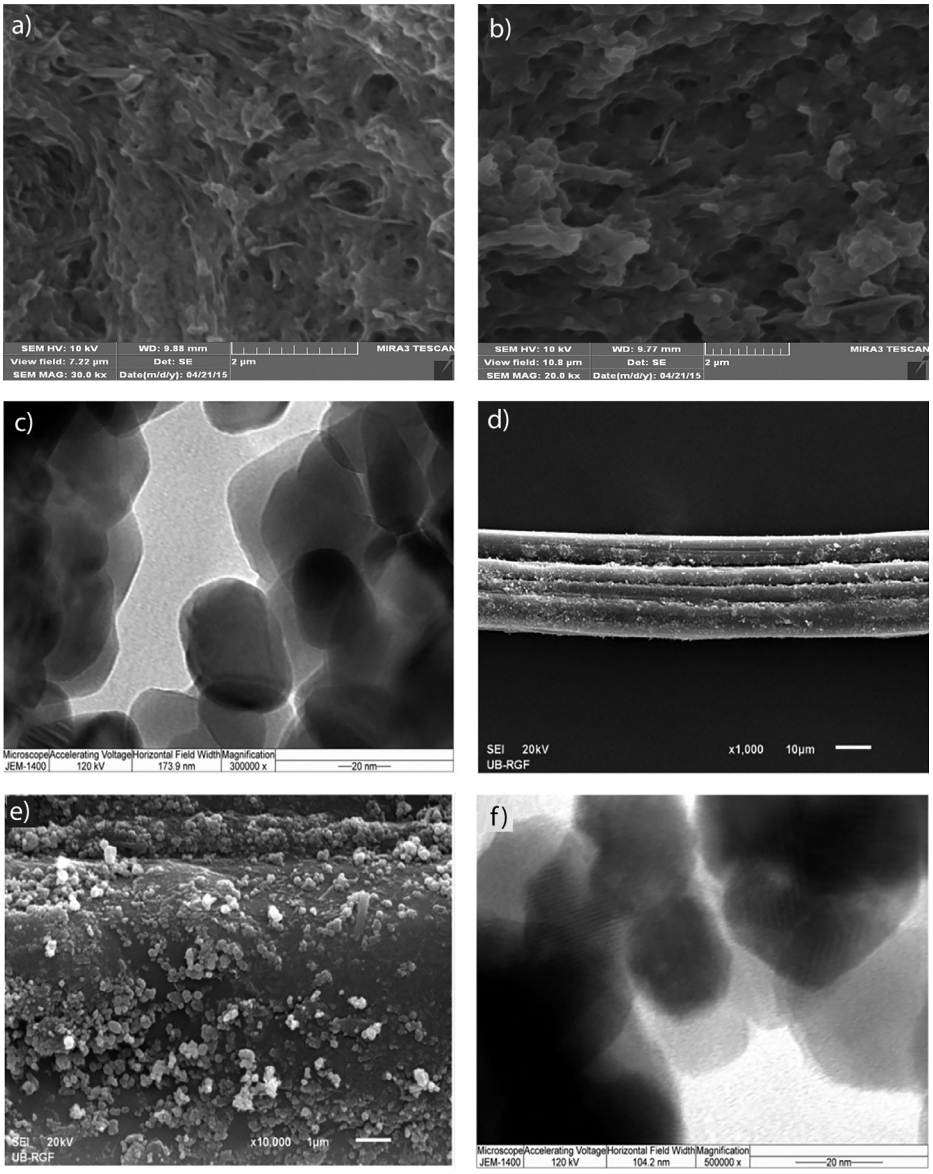

Figure 7 FEG-SEM images of **NC-MA/L** (a), **NC-MA/L-MG** (b), **MC-O/L-MG** (d) and (e); and TEM images of **NC-MA/L-MG** (c) and **MC-O/L-MG** (f).

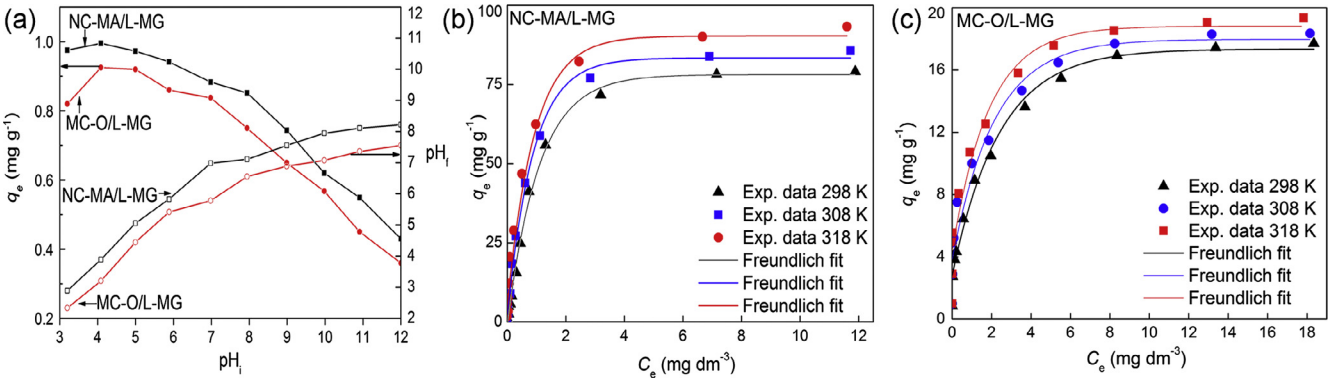

Figure 8 Effect of pH on adsorption of As(V) on **NC-MA/L-MG** and **MC-O/L-MG**, and pH$_f$ *versus* pH$_i$ dependence (a); Freundlich fitting of adsorption data for **NC-MA/L-MG** (b) and **MC-O/L-MG** adsorbents (c).

adsorption data. Statistical criteria (Section 2.11) were used to evaluate the model fitting of adsorption data. Results indicated that the good fitting was obtained by using Langmuir, Eq. (S2), and Freundlich, Eq. (S3), isotherm models.

Adsorption results presented in Fig. 8(b) and (c) and Table 2 showed that good fitting of the experimental data with Freundlich isotherm indicates multilayer adsorption on heterogeneous surfaces. Significantly higher adsorption capacity for **NC-MA/L-MG** (85.3 mg g^{-1}), in comparison with **MC-O/L-MG** (18.5 mg g^{-1}), was obtained by using Langmuir model (Table S2). The favorable textural parameters of **NC-MA/L-MG** contribute to higher arsenate uptake, *i.e.* larger number of available adsorptions sites at nanocomposite surface (Table 1). Somewhat lower capacity was obtained with **NC-MA/L-MG** and **MC-O/L-MG** in a processes of As(III) removal (Table S3), 68.2 and 17.8 mg g^{-1}, respectively. This result is indicated on a wider applicability of synthesized adsorbents. Also, comparative adsorption study of arsenic removal by using **NC-MA/L** showed that 15.4 mg g^{-1} and 4.8 mg g^{-1} were found for As(V) and As(III) at pH 6.0 ± 0.1, respectively. Even lower capacities were obtained for **MC-O/L** (< 6 mg g^{-1} for As(V) removal). These results clearly indicate that validity of the modification of **NC-MA/L** and **MC-O/L** with **MG** was justified by production of high performance **NC-MA/L-MG** and **MC-O/L-MG** adsorbents. Thermodynamic parameters are calculated, according to Eqs. (S4) and (S5) (Vuković et al., 2011), based on adsorption studies performed at different temperatures and calculated K_L Langmuir constant (Table S2), and results are given in Table 2.

The negative value of Gibbs free energy together with positive enthalpy and entropy changes indicates spontaneity and endothermicity of adsorption processes (Table 2). The positive $\Delta H°$ confirms favorable adsorption at higher temperatures. It means that disruption of water hydration shells and transport of arsenic anionic species through the bulk solution, within the pores and through the surface boundary layer are more intensive process at higher temperatures. The transport of exchangeable arsenic oxyanions to adsorption site, and number of (exchangeable) water molecules were released into bulk solution contributing to the increase in entropy change (Markovski et al., 2014a, 2014b). At steady-state condition randomness at adsorbent/solution interface is increased due to different intermolecular interactions which contribute to positive entropy change, *i.e.* adsorption is an entropy-driven process. All of these elementary processes during equilibration contribute to positive enthalpy change. Thermodynamic parameters of both As(V) (Table 2) and As(III) (Table S3) were similar to ones given by Liu et al. (2015).

Preliminary evaluation of the potential of use of both adsorbents **NC-MA/L-MG** and **MC-O/L-MG** for arsenic removal from real water samples, contaminated natural water from the area of the city of Zrenjanin was used (located in Vojvodina, Serbia). Sample used in this work was collected at the point before any purification treatment. Total arsenic concentration, determined by ICP-MS, was found to be 106 μg L^{-1}. Other ionic species of interest present in real water sample are shown in Table 3.

The total arsenic concentration includes following arsenic species: inorganic, As(III) and As(V), and methylated organic arsenic species (monomethylarsenic acid, MMAs(V), and dimethylarsenic acid, DMAs(V)). Due to this it was necessary to perform preliminary determination of present arsenic species. In a previous report we developed simple and efficient method for separation and determination of inorganic arsenic (iAs) and organic arsenic (oAs) in natural water (Issa et al., 2011). Two types of resins were used for determination of

Table 2 Adsorption isotherm (Freundlich) and thermodynamic parameters for arsenate removal.

	T (K)	K_f ((mol/g)(L/mol)$^{1/n}$)	$1/n$	R^2
Freundlich parameters				
MG	298	0.0539 ± 0.0016	0.396 ± 0.012	0.997
	308	0.0473 ± 0.0014	0.480 ± 0.014	0.995
	318	0.0357 ± 0.0012	0.349 ± 0.011	0.993
NC-MA/L-MG	298	0.2412 ± 0.0961	0.562 ± 0.024	0.995
	308	0.2005 ± 0.0802	0.536 ± 0.022	0.994
	318	0.1474 ± 0.0598	0.503 ± 0.020	0.993
MC-O/L-MG	298	0.0032 ± 0.00008	0.188 ± 0.0047	0.995
	308	0.0025 ± 0.00006	0.258 ± 0.0065	0.997
	318	0.0020 ± 0.00005	0.229 ± 0.0057	0.994

	T (K)	$\Delta G°$ (kJ mol^{-1})	$\Delta H°$ (kJ mol^{-1})	$\Delta S°$ (J mol^{-1} K^{-1})	R^2
Thermodynamic parameters					
MG	298	−40.56 ± 0.81	4.31 ± 0.08	150.48 ± 3.01	0.992
	308	−42.05 ± 0.82			
	318	−43.57 ± 0.87			
NC-MA/L-MG	298	−38.66 ± 1.16	10.77 ± 0.32	165.69 ± 4.97	0.978
	308	−40.23 ± 1.21			
	318	−41.98 ± 1.26			
MC-O/L-MG	298	−39.40 ± 0.985	10.99 ± 0.27	168.80 ± 4.22	0.954
	308	−40.90 ± 1.022			
	318	−42.78 ± 1.069			

Table 3 Content of ions[a] in real water samples (mg L^{-1}).

Ions	Concentration in a real water
PO_4^{3-}	5.6
SO_4^{2-}	42.5
Ca^{2+}	15.3
Mg^{2+}	9.1
SiO_4^{4-}	5
Cl^-	1.2
HCO_3^-	856

[a] pH of the sample was 7.4 and it was adjusted to pH 6 ± 0.1.

arsenic species: a strong base anion exchange (SBAE) resin and HY–AgCl based on the activity of silver-chloride loaded on SBAE resin. The SBAE resin has been chosen as a selective resin for the separation of As(V) from As(III), and HY–AgCl for quantitative separation of molecular and ionic forms of iAs and oAs. Molecular form of As(III) that exists in the water at pH < 8.0 was not bonded with SBAE, which was convenient for direct determination of As(III) concentration in the effluent. Experiments performed in a column system filled with HY–AgCl showed that oAs species are not presented in a sample water used. Additional experiment performed in a column system filled with SBAE resin showed that As(III) was present at the level less than 5 μg L^{-1}. In order to perform As(III) oxidation air bubbling for two hours was performed, and determined As(V) in oxidized solution was found to be 104 μg L^{-1}.

Preliminary adsorption study performed with real water sample (Table 3), spiked with 10 mg L^{-1} of As(V), showed 19% decrease in adsorption capacity for **NC-MA/L-MG** (69.1 mg g^{-1}), and 8% for **MC-O/L-MG** (17.0 mg g^{-1}) with respect to experiments performed under non-competitive condition. These results showed possible application of synthesized adsorbents, even in the presence of significant concentration of interfering ions in natural water, in a processes of As(V) removal from groundwater.

3.3.2. *Adsorption kinetics in a non-competitive condition*

Due to complexity of adsorption processes, *i.e.* contribution of mass transfer and chemical reaction, different kinetic models were used to fit experimental data: pseudo-first order, pseudo-second order (PSO), Roginsky-Zeldovich-Elovich, and second-order rate equation. Also diffusion models: liquid film linear driving force rate equation, liquid film diffusion mass transfer rate equation, homogeneous solid diffusion model, Weber-Morris model (WM), Dunwald-Wagner model, and double exponential model (Markovski et al., 2014a, 2014b) were used. PSO and W–M models showed the best fitting (Fig. 9 and Table 4). Additionally, result of comparative kinetic experiments with As(III), and PSO fitting showed higher rate constant, 0.762 ± 0.022 g mg^{-1} min^{-1} for **MC-O/L-MG** at 25 °C, which is an additional evidence of high performances of obtained material.

The results obtained following the W–M model showed three successive linear steps for **MC-O/L-MG**, while two-line correlation lines were obtained for **NC-MA/L-MG** (Fig. 9). Fast kinetics in the first step was followed by medium adsorption rate in the second, and very slow attainment of equilibrium in the third step was found for **MC-O/L-MG**. Higher values of the rate constant, found for **MC-O/L-MG** (Table 4), reflect better diffusibility/easier accessibility of surface active sites by sorbate due to shortening the path of ions inside the adsorbent body.

It is well known that multi-step nature of adsorption processes could be affected by bulk diffusion, boundary layer diffusion, intra-particle diffusion and surface adsorption. The first linear steep part demonstrates external mass transfer from bulk solution to the most available adsorptive sites at outer adsorbent surface. The second and the third parts of the adsorption process significantly depend on adsorbent porosity, *i.e.* pore structure, geometry and network density. Due to the concentration gradient, the ions diffuse through bulk solution and treelike pore system extending into adsorbent interior to reach all available surface active sites (Sun et al., 2014; Yousif et al., 2016). The intra-particle resistance slows down adsorbate transport, *i.e.* net transport in a direction of variable time-dependent concentration gradient. At the final stage, the adsorption takes place at low rate until the saturation of all available surface sites is achieved.

The activation parameters: entropy of activation $\Delta S^{\#}$, Gibbs free energy of activation $\Delta G^{\#}$ and enthalpy of activation $\Delta H^{\#}$ were calculated from kinetic data, obtained at 25, 35, and 45 °C, by using Eqs. (S6)–(S9). The results are presented in Table 4.

The activation energies of 13.28 and 10.87 kJ mol^{-1} for As (V) removal with **NC-MA/L-MG** and **MC-O/L-MG**, respectively, were obtained. These results are in agreement with similar result obtained for synthetic goethite (Lakshmipathiraj et al., 2006). Adsorbate transport is generally controlled by diffusive mass transfer, and thus rates of approaching to equilibrium usually increase with increase in temperature. The results show that the intra-particle diffusion is a rate-controlling step since the activation energy is low and within the range of 8–22 kJ mol^{-1}, characteristic value for diffusion-controlled processes such as ion-exchange/complexation (Haring, 1942).

The improvement of the analysis of kinetic data for whole period of adsorption was performed by applying model free kinetics of adsorption, *i.e.* determination of activation parameters by iso-conversional method. Model free kinetics was selected in order to get the most reliable system responses at appropriate period of time, *i.e.* at the beginning, middle and plateau (approaching to steady state condition) parts of the process. The adsorption rate can be described as the amount of adsorbed pollutant per unit of time by using dimensionless number α. It denotes time-dependent fraction of bounded arsenic, and could be described by Eqs. (S10)–(S13). A plot of $-\ln t$ *versus* $1/T$ at appropriates α yield E_a from the slope regardless of the kinetic/adsorption model was used. The reason for choosing the 'model free' method of kinetic analysis is based on the fact that any misidentification of the kinetic model has got a profound effect on the values obtained for the Arrhenius parameters. Sewry and Brown (2002) and Galwey (2003) have critically reviewed the use of various kinetic models and asserted that caution has to be exercised in choosing the right kinetic model. By applying the fitting of conversion-time data, using predetermined point for calculation of α value, obtained results are presented in Fig. 9(c).

From the slope of correlations Eq. (S12), at appropriate T and α, a series of activation energies data (E_a) were calculated, and results are presented in Fig. 9(c). The plots show that

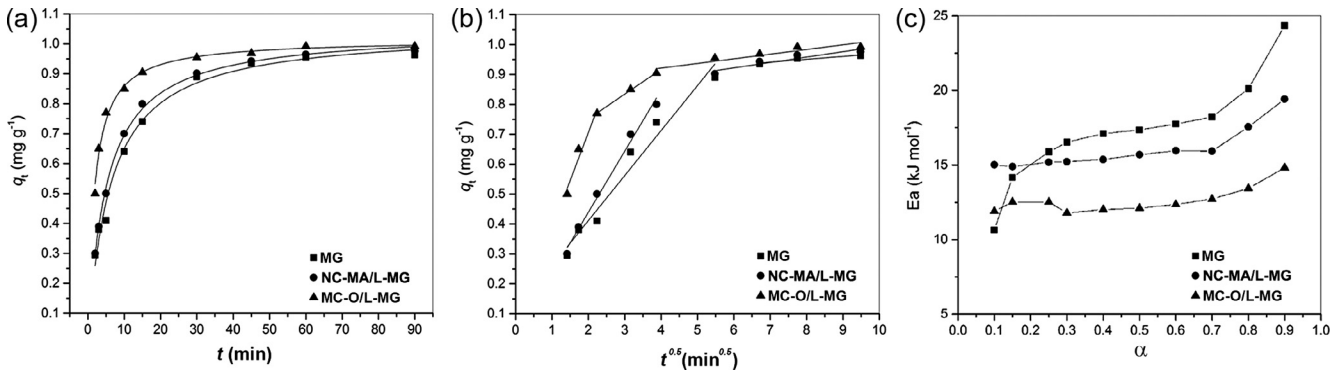

Figure 9 Plot of arsenate adsorption on **MG** by using PSO (a) and WM (b) model at 25 °C (m/V = 100 mg L^{-1}, C_i = 0.1 mg L^{-1}, pH 6.0 ± 0.1), and diagram of activation energies E_a *vs* α c).

Table 4 Kinetic and activation parameters of As(V) removal by using **MG**, **NC-MA/L-MG** and **MC-O/L-MG** adsorbent.

Adsorbent	Pseudo-second-order model			Weber–Morris model						
	q_e (mg g^{-1})	K_2 [a]	R^2	k_{p1} [b]	C (mg g^{-1})	R^2	k_{p2} [b]	R^2	k_{p3} [b]	R^2
MG	1.047 ± 0.024	0.156 ± 0.017	0.985	0.151 ± 0.014	0.110 ± 0.047	0.957	0.0096 ± 0.0035	0.807	–	–
NC-MA/L-MG	1.0463 ± 0.0084	0.189 ± 0.008	0.997	0.204 ± 0.011	0.031 ± 0.030	0.987	0.0181 ± 0.0047	0.829	–	–
MC-O/L-MG	1.0155 ± 0.0095	0.541 ± 0.033	0.989	0.320 ± 0.063	0.065 ± 0.115	0.926	0.0827 ± 0.0025	0.998	0.016 ± 0.004	0.813

	E_a (kJ mol^{-1})	$\Delta H^{\#}_{25}$ (kJ mol^{-1})	$\Delta G^{\#}_{25}$ (kJ mol^{-1})	$\Delta S^{\#}_{25}$ (J mol^{-1} K^{-1})
Activation parameters				
MG	20.10 ± 0.96	17.63 ± 0.86	77.23 ± 3.8	−200.8 ± 9.36
NC-MA/L-MG	13.28 ± 0.65	10.8 ± 0.54	76.96 ± 3.7	−222.5 ± 10.6
MC-O/L-MG	10.87 ± 0.53	8.39 ± 0.42	74.55 ± 3.5	−221.9 ± 10.3

[a] g mg^{-1} min^{-1}.
[b] mg g^{-1} min$^{-0.5}$.

overall adsorption mechanism progressively changed from the initial point of the process to attainment of equilibrium. In general, E_a varies from 15 to 18 kJ mol^{-1} for **NC-MA/L-MG**, and from 12 to 14 kJ mol^{-1} for **MC-O/L-MG**. In the first part of adsorption ($0 < \alpha < 0.3$), the favorable process was noticed for **MG** due to synergetic effect of geometry/surface group density. Afterward, a steady region ($0.3 < \alpha < 0.7$) was attained, and followed by steep increases in the course of equilibration. Similar trend of low change of E_a, for both **NC-MA/L-MG** and **MC-O/L-MG**, was found for $\alpha < 0.7$, and $\alpha > 0.7$, and somewhat higher slope was found for **NC-MA/L-MG**. Generally, the change of *E*a values (Fig. 9) indicates that adsorption is diffusion controlled process, and it is in accordance with the concept of variation of E_a in a real system due to multi-step nature of most processes encountered in practice. The time-dependent change in kinetics is attributed to textural properties, material structure/defects at exposed plane, steric hindrances and electrostatic attraction/repulsion between adsorbed/released molecules/ionic species. The significance of external/internal mass transport and diffusion inside the pores was indicated (Markovski et al., 2014a, 2014b). The obtained activation energy for the As(V) removal with vacuum and freeze dried goethite modified macroporous resin was 18.63 and 20.60 kJ mol^{-1} (Taleb et al., 2015), which indicates that similar phenomena dictate diffusional transport inside morphologically/chemically similar porous system.

3.3.3. Comparison of kinetic/adsorption data of magnetite based adsorbent

Additionally, performance of synthesized adsorbents was evaluated from comparison with other magnetite based adsorbents. Among the large numbers of cellulose based adsorbents synthesized up to date, most of them are claimed and considered to be the best candidates to feasible and applicable for effective arsenic removal. The adequate properties of cellulose based adsorbents, with respect to established criteria in the areas of environmental protection, mainly arise from their low cost and adsorption performances. The literature survey, shown in Table 5, of the data on adsorption kinetics and maximum adsorption capacity of the materials of interest is presented.

The diversity of experimental condition makes impossible convenient overview/comparison of the literature and presented adsorption data. General consideration of the relation of adsorbent performances/textural properties indicates positive dependence of increased surface area with respect to obtained adsorption capacity. According to the results presented (Table 5), the q_{max} was found in a wide range between

Table 5 Adsorption capacity and kinetic data of As(V) removal by using magnetite based/other adsorbents.

Adsorbent	K_2 (g mg^{-1} min^{-1})	Adsorption capacity (mg g^{-1})	References
Magnetite based adsorbent (batch study)			
Magnetite	0.156	**91.2**	This paper
Magnetite	11.33 mg/min	88.4	Lin et al. (2012)
Magnetite/Activated carbon fiber	0.0081	4.16	Zhang et al. (2010)
Magnetite/Starch	–	248	An et al. (2011)
NC-MA/L-MG	0.189	**85.3**	This paper
Cellulose Cu	0.0187	98.9	Yousif et al. (2016)
Amino/G3MA/TiO_2/Cellulose	0.010	108.7	Anirudhan et al. (2012)
Amino/Dianhydride/Cellulose	0.64	12.06	Singh et al. (2015)
Amino/Cellulose	0.029	187	Anirudhan and Jalajamony (2010)
MC-O/NC-L-MG	0.540	**18.5**	This paper
Magnetite/Cellulose fiber	0.00005	2.46	Hokkanen et al. (2015)
PDMAEMA/Cellulose fiber	–	27.9	Tian et al. (2011)
Amino/Cellulose fiber	0.0011	75.1	Yu et al. (2013)
Other adsorbents (column study)			
Zirconium(IV)-loaded monophosphonic acid resin	–	0.0029 mmol/ml	Awual et al. (2011)
Zirconium(IV) loaded fibrous adsorbent	–	0.127 mmol/g	Awual et al. (2012)
Crosslinked poly(allylamine) resin	–	3.5 mmol/g	Awual and Jyo (2009)
Commercial weak-base resins (Diaion WA20)	–	0.239 mmol/g	Awual et al. (2013)
Commercial weak-base resins (Diaion WA30)	–	0.217 mmol/g	Awual et al. (2013)
Weak-base anion exchange fiber	–	0.941 mmol/g	Awual et al. (2008)

Bold values represent results from this work.

2.46 mg g^{-1} for Magnetite/Cellulose fiber and 108.7 mg g^{-1} for Amino/G3MA/TiO_2/Cellulose. The q_{max} obtained from the Langmuir model for the **NC-MA/L-MG** was found to be 85.3 mg g^{-1} at 25 °C, and lower for the **MC-O/L-MG**, 18.5 mg g^{-1} was found, which is comparable to the literature data. It means that synthesized high performance adsorbents offer an acceptable alternative to those published in the literature or eventually used in a real processes, and production of adsorbents based on presented material offers many benefits to existing ones. Fast attainment of adsorption equilibrium, *i.e.*, kinetic rate of arsenic adsorption in the presence of the **MC-O/L-MG** mainly exceeds the values found in the literature (Table 5), and capacity of **NC-MA/L-MG** is similar to those found in the literature. Obtained results are in accordance with general experienced rules on relationship between textural data and adsorbent performance, *i.e.* kinetic and adsorption data. The developed fibers integrated mechanical integrity (stability), hydraulic properties and arsenic selectivity. Despite lower adsorption capacity, another factor contributes to substantial improvement of its performance, and namely the results of adsorption kinetics open an alternative for the use of **MC-O/L-MG** exchange fibers relative to **NC-MA/L-MG** counterparts. The results presented point out to the advantage of application of micro-sized adsorbent which contributes to adsorption performances of chemically identical but physically different materials **NC-MA/L-MG** and **MC-O/L-MG**.

3.3.4. Competitive kinetic study

Except high capacity and fast adsorption rate of arsenic removal, the synthesized adsorbents should possess high affinity/selectivity with respect to selected pollutant. Similar to non-competitive kinetic study, the data obtained in competitive study of arsenate removal in the presence of single interfering ion: SiO_4^{4-}, CrO_4^{2-} and PO_4^{3-} ion were processed by using PSO equation. The other kinetic models were of limited validity to be applied for description of the competitive kinetic study. Therefore, PSO model was used and results of fitting, obtained from plots $q_t - t$ and $t/q_t - t$, are given in Table 6.

On the other hand, calculated values show good agreement with the experimental data for PSO kinetics which means that sorption depends on the both concentration of arsenic and adsorbent surface functionalities. Single competitive As(V) adsorption showed the highest influence of phosphate (11.5% decrease of K_2) for **MG**, 25.9% for **NC-MA/L-MG** and 9.6% for **MC-O/L-MG**. Similar trend but of lower extent was found for chromate and the lowest influence of silicate was noticed. Largest adverse effect showed phosphate due to similar chemistry with arsenate. The acid dissociation constants of phosphoric acid are $p\mathrm{Ka}_1 = 2.16$, $p\mathrm{Ka}_2 = 7.21$ and $p\mathrm{Ka}_3 = 12.32$, which indicates that at pH ~ 6 monovalent phosphate ion, $H_2PO_4^-$, is a dominant competitive species (Awual et al., 2011). Selection of pH 6 in adsorption study was optimal due to an increase in pH, hydroxide concentration increases so that interference of hydroxide with the hardest Lewis acids anion in water increases resulting in decrease in arsenate and phosphate adsorption and phosphate showed lower adsorption capacity at pH 6 than at higher pH on magnetite nanoparticles (Abo Markeb et al., 2016). Among the other interfering ions commonly present in natural water, sulfate, as divalent ions, shows greater competition through enhanced electrostatic interaction. Selection of pH 6, *i.e.* pH ≈ pH_{PZC}, contributes to lower extent of electrostatic interaction of all ions with **MG** surface. Therefore, the main benefit of the designed system adsorbent/adsorption condition arises from achievement of desired levels of arsenate removal in the presence of interfering ions. Silicate showed low effect which was less than 8%.

Except this, experiments performed with **NC-MA/L-MG** in the presence of different concentrations of KCl, KNO_3 (1 and

Table 6 Results of the PSO fitting of As(V) removal in the presence of single interfering ions.

		Non-competitive	Competitive condition		
			SiO_4^{4-}[a]	CrO_4^{2-}[a]	PO_4^{3-}[a]
MG	q_e[b]	1.047(±0.024)	0.998(±0.014)	0.938(±0.014)	0.926(±0.016)
	K_2[c]	0.156(±0.017)	0.144(±0.045)	0.141(±0.040)	0.138(±0.037)
	R^2	0.985	0.989	0.990	0.992
NC-MA/L-MG	q_e	1.046(±0.084)	0.999(±0.013)	0.936(±0.019)	0.918(±0.028)
	K_2	0.189(±0.008)	0.181(± 0.022)	0.179(±0.020)	0.140(±0.027)
	R^2	0.997	0.987	0.989	0.991
MC-O/L-MG	q_e	1.016(±0.010)	0.968(±0.015)	0.932(±0.032)	0.886(±0.029)
	K_2	0.541(±0.033)	0.536(±0.029)	0.519(±0.022)	0.489(±0.0)
	R^2	0.989	0.990	0.982	0.992

[a] C_i = 0.1 mg L^{-1}, m/V = 100 mg L^{-1}, t = 90 min.
[b] mg g^{-1}.
[c] g mg^{-1} min^{-1}.

5 mg L^{-1}), arsenic removal were slightly enhanced. Due to bonding of negatively charged arsenic species, concentration of negative charge is increased in a electrical double layer (Grossl et al., 1997), and at higher ionic strength of solution, increased concentration of counter cations could compensate the surface negative charges. Observed fact that increased ionic strength causes increased arsenate uptake indicating that formation of inner-sphere complexes (Markovski et al., 2014a, 2014b) is the main adsorption mechanism. Additionally, the low influence of interfering ions (Table 6) and pH_{PZC} decreases after adsorption (Table 1) are the properties indicative for the formation of inner-sphere surface complexes. Ligand exchange is a final/crucial step at surface which occurs through formation of monodentate complex, while the next slow step represents a second ligand exchange resulting in the formation of an inner-sphere bidentate binuclear complex (Grossl et al., 1997). Formation of inner-sphere complexes is a process of highest probability, and other types of interaction between As species and protonated hydroxyl groups by forming outer-sphere surface complexation could be operative at lower pH (Liu et al., 2015).

Additionally, competitive kinetic experiments, performed with **NC-MA/L-MG** and **MC-O/L-MG** and natural water sample (Table 3), were carried out to find out the level of the efficiency of total arsenic removal from natural water sample. At 100 mg L^{-1} of **NC-MA/L-MG** 70% of arsenic was removed for 30 min and more than 99% after 60 min. Fast arsenic uptake was obtained with **MC-O/L-MG** adsorbent: 70% removal was achieved for 6 min and after 14 min the total arsenic concentration was below the WHO limit prescribed for arsenic in drinking water. This results showed that at even high concentration of interfering ion (Table 3) fast removal of As(V), present at low level, could be efficiently removed from natural water.

3.3.5. Regeneration versus safety

Experiments related to regeneration study with respect to both **NC-MA/L-MG** and **MC-O/L-MG** adsorbents, and related disposal issue of spent alkali desorption solution are given in Supplementary data.

3.3.6. Future challenges

The adsorption performances, comparable/higher than that of the most common referenced material, observed for well-dispersed/manipulative **NC-MA/L-MG** and **MC-O/L-MG** adsorbents result from the contribution of two factors: (i) design of surface modification with branched organic structure with number of amino terminal groups and (ii) development of controllable method for magnetite precipitation. The main goal of presented study was devoted to understanding of scientific principles related to influences of the parent media size, **NC** *versus* **MC**, on the adsorption properties of produced adsorbents. Also, investigation on the influences of chemical structure/properties of the modified precursor surface on the optimization of the method for magnetite precipitation was an additional goal of this study. Obviously, crystal structure of precipitated magnetite, exposed surface and crystal faces, had pronounced influence on adsorbent properties and strongly depends on experimental condition and **NC/MC** surface properties. It was shown that in a moderately acidic/neutral condition arsenic species are strongly bonded to iron oxide surface. EXAFS analysis suggested predominant formation of bidentate binuclear corner-sharing complexes (^2C) for As(V), with dominant complexes formed between AsO_4^{3-} tetrahedron and two FeO_6 octahedra on {100} surfaces of magnetite (Liu et al., 2015). Also, calculation using density functional theory (DFT) predicted the relative energies and geometries of surface complexes using density functional theory showed higher stability of ^2C complex for 55 kJ mol^{-1} in relation to ^2E edge-sharing bidentate complex (Sherman and Randall, 2003). According to this, good adsorption performances of the novel adsorbents were related to proper **NC** and **MC** modification, and controllable **MG** precipitation which causes beneficial facet evolution at MG surface. As a result, high affinity and efficient arsenate removal from water, as well as acceptable kinetics with possibility for adsorbent use in the processes of natural water remediation even in the presence of competing ions were obtained.

Also, exceptional adsorption performances and magnetic properties of **MG** nanoparticles, precipitated on modified **NC** and **MC** surfaces, provide an opportunity for practical

application and easy separation from aqueous solution by applying external magnetic field. Except this, results of reusability study showed low decrease in adsorption efficiency after five adsorption/desorption cycles (Supplementary data; Section 3.3.5). No measurable iron ion was detected in water during repeated cycles of adsorption. Therefore, **MG** loaded **NC-MA/L** and **MC-O/L** adsorbents could be effectively used for long time of exploitation. Using a proper selection of technology for treatment of spent waste alkali concentrated arsenic provides safe technology for arsenic removal (Supplementary data; Section 3.3.5). In that way, the three main goals were realized by understanding/explaining of scientific principles related to the influences of parent media size, **NC** *versus* **MC**, chemical structure/properties of organic functionalities bonded on **NC** and **MC** surface, and **MG** precipitation method on adsorption performances of novel synthesized adsorbents. Additionally, a number of idea/strategy were designed based on presented results/conclusions, and future work will be focused on development/production of woven nano/-micro cellulose **MG** modified hybrid textile materials.

4. Conclusion

Present study demonstrated that parent media size, functionalities/architecture of organic modifying structure and nanohybrid material have significant influence on adsorption properties of physically different materials. Compared to unsupported **MG**, two novel designed nano and micro cellulose supported adsorbents with organic support (amino functionalized) and inorganic nanohybrid precipitated adsorptive material (magnetite) exhibited favorable adsorption properties toward arsenate. Different geometry (aspect/ratio) and morphological/textural properties caused better adsorptive properties of **NC-MA/L-MG**, *i.e.* nearly five times higher adsorption capacity (85.3 *vs* 18.5 mg g^{-1}) in comparison with **MC-O/L-MG** counterpart. Such results reflect the significance of increased number of amino surface bonding sites, present at **NC-L** surface, which are susceptible for effective **MG** precipitation. The results of kinetic study, for both adsorbents, were well fitted with the PSO and WM kinetic models. However, **MC-O/L-MG** demonstrated significantly faster kinetics, around three times higher value of K_2, 0.541 *vs* 0.189 g mg^{-1} min^{-1}, indicating better availability of surface active sites in **MC-O/L-MG**. Obtained rate constant in the presence of the **MC-O/L-MG** mainly exceeds the values found in the literature, and capacity of **NC-MA/L-MG** is similar/higher to literature data which confirms high applicability of both adsorbents. Iso-conversional method applied on kinetic data of both adsorbents showed that **MC-O/L-MG** was preferable material due to lower dependence of E_a on the extent of adsorption. Additionally, both adsorbents showed applicability in a competitive condition, reusability and possibility for separation of saturated adsorbent by magnetic field.

Acknowledgment

The authors acknowledge financial support from Ministry of Education, Science and Technological developments of the Republic of Serbia, Projects Nos. OI 172057 and III45019.

Appendix A. Supplementary material

Supplementary data associated with this article can be found, in the online version, at http://dx.doi.org/10.1016/j.arabjc.2016.08.006.

References

Abdel-Halim, E.S., Al-Deyab, S.S., 2011. Removal of heavy metals from their aqueous solutions through adsorption onto natural polymers. Carbohydr. Polym. 84, 454–458. http://dx.doi.org/10.1016/j.carbpol.2010.12.001.

Abo Markeb, A., Alonso, A., Dorado, A.D., Sánchez, A., Font, X., 2016. Phosphate removal and recovery from water using nanocomposite of immobilized magnetite nanoparticles on cationic polymer. Environ. Technol. 37, 2099–2112. http://dx.doi.org/10.1080/09593330.2016.1141999.

Alila, S., Boufi, S., 2009. Removal of organic pollutants from water by modified cellulose fibres. Ind. Crops Prod. 30, 93–104. http://dx.doi.org/10.1016/j.indcrop.2009.02.005.

Aloulou, F., Boufi, S., Labidi, J., 2006. Modified cellulose fibres for adsorption of organic compound in aqueous solution. Sep. Purif. Technol. 52, 332–342. http://dx.doi.org/10.1016/j.seppur.2006.05.008.

An, B., Liang, Q., Zhao, D., 2011. Removal of arsenic(V) from spent ion exchange brine using a new class of starch-bridged magnetite nanoparticles. Water Res. 45, 1961–1972. http://dx.doi.org/10.1016/j.watres.2011.01.004.

Anirudhan, T.S., Deepa, Binusreejayan, J.R., 2015. Synthesis and characterization of multi-carboxyl-functionalized nanocellulose/nanobentonite composite for the adsorption of uranium(VI) from aqueous solutions: kinetic and equilibrium profiles. Chem. Eng. J. 273, 390–400. http://dx.doi.org/10.1016/j.cej.2015.03.007.

Anirudhan, T.S., Jalajamony, S., 2010. Cellulose-based anion exchanger with tertiary amine functionality for the extraction of arsenic(V) from aqueous media. J. Environ. Manage. 91, 2201–2207. http://dx.doi.org/10.1016/j.jenvman.2010.05.019.

Anirudhan, T.S., Nima, J., Sandeep, S., Ratheesh, V.R.N., 2012. Development of an amino functionalized glycidylmethacrylate-grafted-titanium dioxide densified cellulose for the adsorptive removal of arsenic(V) from aqueous solutions. Chem. Eng. J. 209, 362–371. http://dx.doi.org/10.1016/j.cej.2012.07.129.

Awual, M.R., 2016a. Assessing of lead(III) capturing from contaminated wastewater using ligand doped conjugate adsorbent. Chem. Eng. J. 289, 65–73. http://dx.doi.org/10.1016/j.cej.2015.12.078.

Awual, M.R., 2016b. Solid phase sensitive palladium(II) ions detection and recovery using ligand based efficient conjugate nanomaterials. Chem. Eng. J. 300, 264–272. http://dx.doi.org/10.1016/j.cej.2016.04.071.

Awual, M.R., 2016c. Ring size dependent crown ether based mesoporous adsorbent for high cesium adsorption from wastewater. Chem. Eng. J. 303, 539–546. http://dx.doi.org/10.1016/j.cej.2016.06.040.

Awual, M.R., 2015. A novel facial composite adsorbent for enhanced copper(II) detection and removal from wastewater. Chem. Eng. J. 266, 368–375. http://dx.doi.org/10.1016/j.cej.2014.12.094.

Awual, M.R., El-Safty, S.A., Jyo, A., 2011. Removal of trace arsenic (V) and phosphate from water by a highly selective ligand exchange adsorbent. J. Environ. Sci. 23, 1947–1954. http://dx.doi.org/10.1016/S1001-0742(10)60645-6.

Awual, M.R., Hossain, M.A., Shenashen, M.A., Yaita, T., Suzuki, S., Jyo, A., 2013. Evaluating of arsenic(V) removal from water by weak-base anion exchange adsorbents. Environ. Sci. Pollut. Res. 20, 421–430. http://dx.doi.org/10.1007/s11356-012-0936-7.

Awual, M.R., Jyo, A., 2009. Rapid column-mode removal of arsenate from water by crosslinked poly(allylamine) resin. Water Res. 43, 1229–1236. http://dx.doi.org/10.1016/j.watres.2008.12.018.

Awual, M.R., Miyazaki, Y., Taguchi, T., Shiwaku, H., Yaita, T., 2016a. Encapsulation of cesium from contaminated water with highly selective facial organic–inorganic mesoporous hybrid adsorbent. Chem. Eng. J. 291, 128–137. http://dx.doi.org/10.1016/j.cej.2016.01.109.

Awual, M.R., Shenashen, M.A., Yaita, T., Shiwaku, H., Jyo, A., 2012. Efficient arsenic(V) removal from water by ligand exchange fibrous adsorbent. Water Res. 46, 5541–5550. http://dx.doi.org/10.1016/j.watres.2012.07.038.

Awual, M.R., Urata, S., Jyo, A., Tamada, M., Katakai, A., 2008. Arsenate removal from water by a weak-base anion exchange fibrous adsorbent. Water Res. 42, 689–696. http://dx.doi.org/10.1016/j.watres.2007.08.020.

Awual, M.R., Yaita, T., Miyazaki, Y., Matsumura, D., Shiwaku, H., Taguchi, T., 2016b. A reliable hybrid adsorbent for efficient radioactive cesium accumulation from contaminated wastewater. Sci. Rep. 6, 19937. http://dx.doi.org/10.1038/srep19937.

Cabaniss, S.E., 2011. Forward modeling of metal complexation by NOM: II. Prediction of binding site properties. Environ. Sci. Technol. 45, 3202–3209. http://dx.doi.org/10.1021/es102408w.

Donia, A.M., Atia, A.A., Abouzayed, F.I., 2012. Preparation and characterization of nano-magnetic cellulose with fast kinetic properties towards the adsorption of some metal ions. Chem. Eng. J. 191, 22–30. http://dx.doi.org/10.1016/j.cej.2011.08.034.

Dufresne, A., 2012. Nanocellulose: from nature to high performance tailored materials. De Gruyter Germany.

Erdem, E., Karapinar, N., Donat, R., 2004. The removal of heavy metal cations by natural zeolites. J. Colloid Interface Sci. 280, 309–314. http://dx.doi.org/10.1016/j.jcis.2004.08.028.

Foo, K.Y., Hameed, B.H., 2010. Insights into the modeling of adsorption isotherm systems. Chem. Eng. J. 156, 2–10. http://dx.doi.org/10.1016/j.cej.2009.09.013.

Gabelica, Ž., 1976. Vibrational studies of metal-ethylenediamine thiosulfates – I. Infrared and Raman spectra of the tris-ethylenediamine thiosulfates $M^{II}(en)_3S_2O_3$(M^{II} = Zn, Cd, Fe, Ni Co, Mn) and some of their N-deuterated analogues. Spectrochica Acta 32, 327–336. http://dx.doi.org/10.1016/0584-8539(76)80085-2.

Galwey, A.K., 2003. Eradicating erroneous Arrhenius arithmetic. Thermochim. Acta 399, 1–29. http://dx.doi.org/10.1016/S0040-6031(02)00465-3.

Grossl, P.R., Eick, M., Sparks, D.L., Goldberg, S., Ainsworth, C.C., 1997. Kinetic evaluation using a pressure-jump relaxation technique. Environ. Sci. Technol. 31, 321–326. http://dx.doi.org/10.1021/es950654l.

Haring, M.M., 1942. The theory of rate processes (Glasstone, Samuel; Laidler, Keith J.; Eyring, Henry). J. Chem. Educ. 19, 249. http://dx.doi.org/10.1021/ed019p249.1.

Hokkanen, S., Bhatnagar, A., Repo, E., Lou, S., Sillanpää, M., 2016. Calcium hydroxyapatite microfibrillated cellulose composite as a potential adsorbent for the removal of Cr(VI) from aqueous solution. Chem. Eng. J. 283, 445–452. http://dx.doi.org/10.1016/j.cej.2015.07.035.

Hokkanen, S., Repo, E., Lou, S., Sillanpää, M., 2015. Removal of arsenic(V) by magnetic nanoparticle activated microfibrillated cellulose. Chem. Eng. J. 260, 886–894. http://dx.doi.org/10.1016/j.cej.2014.08.093.

Hua, M., Zhang, S., Pan, B., Zhang, W., Lv, L., Zhang, Q., 2012. Heavy metal removal from water/wastewater by nanosized metal oxides: a review. J. Hazard. Mater. 211–212, 317–331. http://dx.doi.org/10.1016/j.jhazmat.2011.10.016.

Huang, Z., Wu, Q., Liu, S., Liu, T., Zhang, B., 2013. A novel biodegradable β-cyclodextrin-based hydrogel for the removal of heavy metal ions. Carbohydr. Polym. 97, 496–501. http://dx.doi.org/10.1016/j.carbpol.2013.04.047.

Issa, N.Ben., Rajaković-Ognjanović, V.N., Marinković, A.D., Rajaković, L.V., 2011. Separation and determination of arsenic species in water by selective exchange and hybrid resins. Anal. Chim. Acta 706, 191–198. http://dx.doi.org/10.1016/j.aca.2011.08.015.

Jaeger, D.A., Jose, R., Mendoza, A., Apkarian, R.P., 2007. Surfactant transition metal chelates. Colloids Surfaces A Physicochem. Eng. Asp. 302, 186–196. http://dx.doi.org/10.1016/j.colsurfa.2007.02.021.

Klemm, D., Kramer, F., Moritz, S., Lindström, T., Ankerfors, M., Gray, D., Dorris, A., 2011. Nanocelluloses: a new family of nature-based materials. Angew. Chemie Int. Ed. 50, 5438–5466. http://dx.doi.org/10.1002/anie.201001273.

Lakshmipathiraj, P., Narasimhan, B.R.V., Prabhakar, S., Bhaskar Raju, G., 2006. Adsorption of arsenate on synthetic goethite from aqueous solutions. J. Hazard. Mater. 136, 281–287. http://dx.doi.org/10.1016/j.jhazmat.2005.12.015.

Lavoine, N., Desloges, I., Dufresne, A., Bras, J., 2012. Microfibrillated cellulose – its barrier properties and applications in cellulosic materials: a review. Carbohydr. Polym. 90, 735–764. http://dx.doi.org/10.1016/j.carbpol.2012.05.026.

Li, Y., Cao, L., Li, L., Yang, C., 2015. In situ growing directional spindle TiO_2 nanocrystals on cellulose fibers for enhanced $Pb^{(2+)}$ adsorption from water. J. Hazard. Mater. 289, 140–148. http://dx.doi.org/10.1016/j.jhazmat.2015.02.051.

Lin, S., Lu, D., Liu, Z., 2012. Removal of arsenic contaminants with magnetic γ-Fe_2O_3 nanoparticles. Chem. Eng. J. 211–212, 46–52. http://dx.doi.org/10.1016/j.cej.2012.09.018.

Liu, C.-H., Chuang, Y.-H., Chen, T.-Y., Tian, Y., Li, H., Wang, M.-K., Zhang, W., 2015. Mechanism of arsenic adsorption on magnetite nanoparticles from water: thermodynamic and spectroscopic studies. Environ. Sci. Technol. 49, 7726–7734. http://dx.doi.org/10.1021/acs.est.5b00381.

Lu, P., Hsieh, Y.-L., 2010. Preparation and properties of cellulose nanocrystals: rods, spheres, and network. Carbohydr. Polym. 82, 329–336. http://dx.doi.org/10.1016/j.carbpol.2010.04.073.

Maiti, S., Jayaramudu, J., Das, K., Reddy, S.M., Sadiku, R., Ray, S.S., Liu, D., 2013. Preparation and characterization of nano-cellulose with new shape from different precursor. Carbohydr. Polym. 98, 562–567. http://dx.doi.org/10.1016/j.carbpol.2013.06.029.

Maliyekkal, S.M., Lisha, K.P., Pradeep, T., 2010. A novel cellulose–manganese oxide hybrid material by in situ soft chemical synthesis and its application for the removal of Pb(II) from water. J. Hazard. Mater. 181, 986–995. http://dx.doi.org/10.1016/j.jhazmat.2010.05.112.

Markovski, J.S., Đokić, V., Milosavljević, M., Mitrić, M., Perić-Grujić, A.A., Onjia, A.E., Marinković, A.D., 2014a. Ultrasonic assisted arsenate adsorption on solvothermally synthesized calcite modified by goethite, α-MnO_2 and goethite/α-MnO_2. Ultrason. Sonochem. 21, 790–801. http://dx.doi.org/10.1016/j.ultsonch.2013.10.006.

Markovski, J.S., Marković, D.D., Dokić, V.R., Mitrić, M., Ristić, M. D., Onjia, A.E., Marinković, A.D., 2014b. Arsenate adsorption on waste eggshell modified by goethite, α-MnO_2 and goethite/α-MnO_2. Chem. Eng. J. 237, 430–442. http://dx.doi.org/10.1016/j.cej.2013.10.031.

Peng, Y., Gardner, D.J., Han, Y., Kiziltas, A., Cai, Z., Tshabalala, M. a., 2013. Influence of drying method on the material properties of nanocellulose I: thermostability and crystallinity. Cellulose 20, 2379–2392. http://dx.doi.org/10.1007/s10570-013-0019-z.

Podder, M.S., Majumder, C.B., 2019. Bacteria immobilization on neem leaves/$MnFe_2O_4$ composite surface for removal of As(III) and As(V) from wastewater. Arab. J. Chem. 12 (8), 3263–3288.

Przepiera, K., Przepiera, A., 2001. Kinetics of thermal transformations of precipitated magnetite and goethite. J. Therm. Anal. Calorim. 65, 497–503. http://dx.doi.org/10.1023/A:1012441421955.

Ravenscroft, P., Brammer, H., Richards, K., 2009. Arsenic Pollution: A Global Synthesis. John Wiley & Sons, United Kingdom.

Schenzel, K., Fischer, S., 2001. NIR FT Raman spectroscopy – a rapid analytical tool for detecting the transformation of cellulose polymorphs. Cellulose 8, 49–57. http://dx.doi.org/10.1023/A:1016616920539.

Schenzel, K., Fischer, S., Brendler, E., 2005. New method for determining the degree of cellulose I crystallinity by means of FT Raman spectroscopy. Cellulose 12, 223–231. http://dx.doi.org/10.1007/s10570-004-3885-6.

Schwaminger, S.P., García, P.F., Merck, G.K., Bodensteiner, A., Heissler, S., Günther, S., Berensmeier, S., 2015. On the nature of interactions of amino acids with bare magnetite nanoparticles. doi: http://dx.doi.org/10.1021/acs.jpcc.5b07195.

Schwertmann, U., Cornell, R.M., 2000. Iron Oxides in the Laboratory, 2nd ed. Wiley-VCH, Weinheim.

Sewry, J.D., Brown, M.E., 2002. "Model-free" kinetic analysis? Thermochim. Acta 390, 217–225.

Shebanova, O.N., Lazor, P., 2003. Raman spectroscopic study of magnetite ($FeFe_2O_4$): a new assignment for the vibrational spectrum. J. Solid State Chem. 174, 424–430. http://dx.doi.org/10.1016/S0022-4596(03)00294-9.

Sheng, T., Baig, S.A., Hu, Y., Xue, X., Xu, X., 2014. Development, characterization and evaluation of iron-coated honeycomb briquette cinders for the removal of As(V) from aqueous solutions. Arab. J. Chem. 7, 27–36. http://dx.doi.org/10.1016/j.arabjc.2013.05.032.

Sherman, D.M., Randall, S.R., 2003. Surface complexation of arsenic (V) to iron(III) (hydr)oxides: structural mechanism from ab initio molecular geometries and EXAFS spectroscopy. Geochim. Cosmochim. Acta 67, 4223–4230. http://dx.doi.org/10.1016/S0016-7037(03)00237-0.

Šimkovic, I., 2013. Unexplored possibilities of all-polysaccharide composites. Carbohydr. Polym. 95, 697–715. http://dx.doi.org/10.1016/j.carbpol.2013.03.040.

Singh, K., Sinha, T.J.M., Srivastava, S., 2015. Functionalized nanocrystalline cellulose: smart biosorbent for decontamination of arsenic. Int. J. Miner. Process. 139, 51–63. http://dx.doi.org/10.1016/j.minpro.2015.04.014.

Socrates, G., 2004. Infrared and Raman Characteristic Group Frequencies: Tables and Charts. John Wiley & Sons.

Sun, X., Yang, L., Li, Q., Zhao, J., Li, X., Wang, X., Liu, H., 2014. Amino-functionalized magnetic cellulose nanocomposite as adsorbent for removal of Cr(VI): synthesis and adsorption studies. Chem. Eng. J. 241, 175–183. http://dx.doi.org/10.1016/j.cej.2013.12.051.

Szymańska-Chargot, M., Cybulska, J., Zdunek, A., 2011. Sensing the structural differences in cellulose from apple and bacterial cell wall materials by Raman and FT-IR spectroscopy. Sensors 11, 5543–5560. http://dx.doi.org/10.3390/s110605543.

Taleb, K., Markovski, J., Milosavljević, M., Marinović-Cincović, M., Rusmirović, J., Ristić, M., Marinković, A., 2015. Efficient arsenic removal by cross-linked macroporous polymer impregnated with hydrous iron oxide: material performance. Chem. Eng. J. 279, 66–78. http://dx.doi.org/10.1016/j.cej.2015.04.147.

Tian, Y., Wu, M., Liu, R., Wang, D., Lin, X., Liu, W., Ma, L., Li, Y., Huang, Y., 2011. Modified native cellulose fibers – a novel efficient adsorbent for both fluoride and arsenic. J. Hazard. Mater. 185, 93–100. http://dx.doi.org/10.1016/j.jhazmat.2010.09.001.

Vuković, G.D., Marinković, A.D., Škapin, S.D., Ristić, M.T., Aleksić, R., Perić-Grujić, A.a., Uskoković, P.S., 2011. Removal of lead from water by amino modified multi-walled carbon nanotubes. Chem. Eng. J. 173, 855–865. http://dx.doi.org/10.1016/j.cej.2011.08.036.

Wiley, J.H., Atalla, R.H., 1987. Band assignments in the Raman spectra of celluloses. Carbohydr. Res. 160, 113–129. http://dx.doi.org/10.1016/0008-6215(87)80306-3.

Yousif, A.M., Zaid, O.F., Ibrahim, I.A., 2016. Fast and selective adsorption of As(V) on prepared modified cellulose containing Cu (II) moieties. Arab. J. Chem. 9 (5), 607–615.

Yu, X., Tong, S., Ge, M., Wu, L., Zuo, J., Cao, C., Song, W., 2013. Synthesis and characterization of multi-amino-functionalized cellulose for arsenic adsorption. Carbohydr. Polym. 92, 380–387. http://dx.doi.org/10.1016/j.carbpol.2012.09.050.

Zeng, L., Chen, Y., Zhang, Q., Guo, X., Peng, Y., Xiao, H., Chen, X., Luo, J., 2015. Adsorption of Cd(II), Cu(II) and Ni(II) ions by cross-linking chitosan/rectorite nano-hybrid composite microspheres. Carbohydr. Polym. 130, 333–343. http://dx.doi.org/10.1016/j.carbpol.2015.05.015.

Zhang, K., Feldner, A., Fischer, S., 2011. FT Raman spectroscopic investigation of cellulose acetate. Cellulose 18, 995–1003. http://dx.doi.org/10.1007/s10570-011-9545-8.

Zhang, S., Li, X.Y., Chen, J.P., 2010. Preparation and evaluation of a magnetite-doped activated carbon fiber for enhanced arsenic removal. Carbon N. Y. 48, 60–67. http://dx.doi.org/10.1016/j.carbon.2009.08.030.

Zhao, Y., Huang, M., Wu, W., Jin, W., 2009. Synthesis of the cotton cellulose based Fe(III)-loaded adsorbent for arsenic(V) removal from drinking water. Desalination 249, 1006–1011. http://dx.doi.org/10.1016/j.desal.2009.09.015.